LOCALIZING SAGITTARIUS A* AND M87 ON MICROARCSECOND SCALES WITH MILLIMETER VLBI

AVERY E. BRODERICK¹, ABRAHAM LOEB² AND MARK J. REID³

Canadian Institute for Theoretical Astrophysics, 60 St. George St., Toronto, ON M5S 3H8, Canada; aeb@cita.utoronto.ca
 Institute for Theory and Computation, Harvard University, Center for Astrophysics, 60 Garden St., Cambridge, MA 02138.
 Harvard-Smithsonian Center for Astrophysics, 60 Garden St., Cambridge, MA 02138.
 Draft version May 24, 2021

ABSTRACT

With the advent of the *Event Horizon Telescope* (EHT), a millimeter/sub-millimeter very-long baseline interferometer (VLBI), it has become possible to image a handful of black holes with sub-horizon resolutions. However, these images do not translate into microarcsecond absolute positions due to the lack of absolute phase information when an external phase reference is not used. Due to the short atmospheric coherence time at these wavelengths, nodding between the source and phase reference is impractical. However, here we suggest an alternative scheme which makes use of the fact that many of the VLBI stations within the EHT are arrays in their own right. With this we show that it should be possible to absolutely position the supermassive black holes at the centers of the Milky Way (Sgr A*) and M87 relative to nearby objects with precisions of roughly $1\,\mu$ as. This is sufficient to detect the perturbations to Sgr A*'s position resulting from interactions with the stars and stellar-mass black holes in the Galactic cusp on year timescales, and severely constrain the astrophysically relevant parameter space for an orbiting intermediate mass black hole, implicated in some mechanisms for producing the young massive stars in the Galactic center. For M87, it allows the registering of millimeter images, in which the black hole may be identified by its silhouette against nearby emission, and existing larger scale radio images, eliminating present ambiguities in the nature of the radio core and inclination, opening angle, and source of the radio jet.

Subject headings: Black hole physics — Galaxy: center — Techniques: interferometric — Submillimeter: general — Astrometry — Proper motions

1. INTRODUCTION

The Event Horizon Telescope (EHT), a proposed Earth-sized array of existing millimeter and sub-millimeter observatories, promises to provide microarcsecond imaging resolutions via very-long baseline interferometry (VLBI) (Doeleman et al. 2009a). This is sufficient to resolve the horizons of a handful of supermassive black holes, including Sagittarius A* (Sgr A*) and M87. Already, a mm-VLBI array consisting of three stations has probed sub-horizon scale structure in Sgr A* at 1.3 mm wavelengths (Doeleman et al. 2008; Fish et al. 2011). These have been used to test fundamental physics, providing direct evidence for the existence of an event horizon surrounding the supermassive black hole at the center of the Milky Way (Broderick et al. 2009b), as well as study the accretion flow surround Sgr A*, giving an estimate for the black hole spin (Broderick et al. 2009a; Huang et al. 2009; Mościbrodzka et al. 2009; Dexter et al. 2010; Broderick et al. 2010).

The existing observations have made use of the James Clerk Maxwell Telescope (JCMT) and the Sub-Millimeter Array (SMA), located atop Mauna Kea in Hawaii, the Combined Array for Research in Millimeter-wave Astronomy (CARMA) in Cedar Flat, California, and the Arizona Radio Observatory Sub-Millimeter Telescope (SMT) on Mount Graham, Arizona, giving a maximum baseline of 4500km, oriented predominantly east-west. Potential future stations include sites in Chile (Atacama Pathfinder EXperiment, Atacama Submillimeter Telescope and Atacama Large Millimeter Array; APEX, ASTE, and ALMA, respectively), Mexico (Large Millimeter Telescope; LMT), the South Pole (South Pole Telescope; SPT), and the IRAM telescopes in Spain (Pico Veleta; PV) and France (Plateau de Bure; PdB). Among these the longest baselines are $\simeq 1.2 \times 10^4$ km, corresponding to a synthesized beam of 30μ as at 230 GHz (1.3 mm) and 20μ as at 345 GHz $(0.87 \, \text{mm}).$

In addition to including new baselines, improvements in sensitivity are actively being pursued, both by pushing towards larger bandwidths and collecting areas. Using the JCMT, SMT and a single 10 m antenna at CARMA, Fish et al. (2011) was able to measure 0.1 Jy visibilities on long baselines. Efforts already underway to increase the bandwidth to 4 GHz will improve that by a factor of two. Phasing together the multiple telescopes on Mauna Kea (SMA, JCMT & CSO; Weintroub 2008) and many antenna at CARMA will improve this further, increasing sensitivity by a factor of 3 at some sites, making it possible to detect sources considerably dimmer than Sgr A* and M87. This will make it possible to contemplate doing astrometry on microarcsecond scales using the EHT.

Since the advent of self-calibration, phased-reference VLBI observations have only been necessary in imaging observations for low-brightness sources. Nevertheless, because the use of closure phases discards an over-all phase calibration, phasereferenced observations provide the unique capability to do relative astrometry between distinct sources, e.g., positioning a target relative to distant background quasars. In the case of the Galactic Center, 7 mm-VLBI observations using the Very-Long Baseline Array have already paid substantial scientific dividends: placing tight constraints upon the motion of Sgr A* (Reid et al. 1999a; Reid & Brunthaler 2004; Reid et al. 2008), providing independent parallax measurements of our distance from the Galactic center (Reid et al. 2009), and registering the radio and infrared reference frames of the central 0.1 pc (Menten et al. 1997; Reid et al. 2003, 2007). All of these make specific use of background quasars to locate sources within the Galactic center to sub-milliarcsecond precisions.

Moving towards shorter wavelengths is challenging for a number of reasons, including the typically rapidly declining source flux densities and shortened atmospheric coherence time (10 s) and angle (isoplanatic angle, $\sim 3^\circ$, see Appendix A). Nevertheless, there are strong scientific motivations for attempting to do so. Chief among these is that at mm-wavelengths the detection of the black hole silhouette unambiguously identifies and locates the supermassive black holes in Sgr A* and M87. Registering the mm and cm-VLBI reference frames then provides a means to determine where the black hole is relative to larger morphological features. Microarcsecond astrometry also allows the direct detection of the jitter induced by the interaction of the supermassive black holes with the retinue of compact objects in their vicinity, providing a probe of the dark component of the stellar cusp surrounding the central object. Finally, absolute astrometry makes it possible to study short-timescale morphological changes in Sgr A* and M87.

Here we describe some of the the scientific motivations for phase-referenced mm-VLBI in more detail, giving estimates of characteristic time scales and precisions needed to detect the relevant phenomena. Since the particular questions that are accessible are different in Sgr A* and M87, we will address each separately. Section 2 describes a possible scheme by which mm-VLBI may be accomplished, including some of the critical limitations that the short wavelength imposes. Sections 3 and 4 provide the motivations as well as candidate phase references that meet the requirements set out in Section 2. Finally, concluding remarks may be found in Section 5.

2. PHASE REFERENCED MILLIMETER-VLBI

With the advent of self-calibration, interferometric radio observations became capable of reconstructing the vast majority of complex visibility phase information in a given observation, correcting for the nearly all of the station-dependent errors due to propagation through the atmosphere. These methods are, however, insensitive to an overall phase shift of the complex visibilities, including to a translational uncertainty in the image. This precludes VLBI observations from measuring the absolute position of radio features at the incredible precision that it can image them.

This situation may be ameliorated with the use of a phase reference, which provides a fixed point against which to measure the relative location of the source. For this purpose, background quasars are frequently used, due to their small intrinsic angular size, high brightness and exceedingly small transverse velocities. In practice, the small angular size and fixed location of the phase reference provides an easily modeled system with which to reconstruct with high accuracy the phase errors at each VLBI station, fulfilling an analogous role as guide stars in optical and infrared adaptive optics systems¹.

Any potential phase reference must be sufficiently close to the target that it suffers strongly correlated phase distortions, i.e., it must lie within the isoplanatic patch. At mm-wavelengths this depends upon the particular site, typically requiring separations $\lesssim 2^{\circ}-3^{\circ}$, though we will discuss this in more detail below (see also Appendix A). Similarly, the phase reference must be detectable on timescales comparable to the atmospheric coherence time, roughly 10s at mm-wavelengths. In practice, these impose severe limitations on phase-referenced mm-VLBI. While a handful of potential phase references may exist within 2° of the target source, none

 Table 1

 EHT Baseline Sensitivities for Multi-Antenna Stations

Realization	Baseline	$F_{230}(\text{mJy})$	F ₃₄₅ (mJy)	$F_{230,0}^{M}(Jy)$	$F_{345,0}^{M}(Jy)$
EHT-I	$H^{J}-C^{1}$	41	63	1.3	1.7
_	$H^{J}-A^{1}$	19	34	0.61	0.91
_	C^1 $-A^1$	27	45	0.88	1.2
	P^1-A^1	17	36	0.56	0.94
EHT-C	H^a-C^8	10	16	0.33	0.42
	$H^a - A^{10}$	3.9	7.1	0.13	0.19
	$C^7 - A^{10}$	3.3	5.5	0.11	0.15
_	P^6-A^{10}	2.2	4.6	0.072	0.12

lie within the beam widths of individual EHT stations, which range from 6" (LMT) to 54" (SMA). As a consequence, observations of the target source and phase reference with a single dish requires repointing the telescopes. However, this must be accomplished well within the atmospheric coherence time, leaving sufficient time to detect both the source and the phase reference, something that is presently not possible.

However, the EHT is unique in that many of the VLBI stations are interferometers in their own right, i.e., contain many independent antennas. As a consequence, at these stations it is possible to observe both the target source and phase reference simultaneously using a subset of the available antennas for each (the *Paired Antennas* approach described in Chapter 13.2 of Thompson et al. 2001). The remaining instrumental components of the complex gains change slowly in comparison to the atmospheric propagation effects, and thus may be measured by periodically switching antennas from one subset to the other. This is identical to the approach used by Counselman et al. (1974) to detect the gravitational deflection of quasars via VLBI, and similar to the principles underlying VERA (Kawaguchi et al. 2000; Honma et al. 2000).

Stations consisting of arrays are some of the most sensitive in the EHT, providing the most permissive flux limits upon potential phase references. Potential stations for this purpose include Hawaii, CARMA, ALMA and Plateau de Bure. The limiting sensitivities at 230 GHz and 345 GHz on baselines that include these stations at both ends, assuming a bandwidth of 4 GHz and 10s integration times, are listed in Table 1. We include sensitivity estimates for two possible realization:

EHT-I: Using only the JCMT in Hawaii (H^J), a single 10.4 m antenna at CARMA (C¹), 12 m antenna at ALMA (A¹), and a single 15 m antenna at Plateau de Bure (P¹).

EHT-C: Using the phased Hawaii station (including the SMA, JCMT and CSO, H^a), 8 CARMA antennas (6 10.4 m and 2 6.1 m antennas, C⁸), 10 12 m ALMA antennas (A¹⁰) and all 6 15 m Plateau de Bure antennas (P⁶).

The first of these indicate what is possible with limited number of antenna, similar to what is possible for initial version of the EHT, available in the near future. The second corresponds to the maximum achievable sensitivities using the complete EHT though employing only existing facilities. To estimate these flux limits we used the system-equivalent flux densities reported in Doeleman et al. (2009b)

In Appendix A we estimate the atmospheric limits upon the accuracy with which angular separation may be measured. In principle, this is also limited by source structure and variability, though imaging with the EHT should ameliorate these (indeed, as described in Section 3.1.4 the characterization of source

¹ In this context, when we refer to "phase-referenced mm-VLBI" we are not describing a scheme for performing mm-VLBI observations on dim sources. Rather, we are discussing a means to assess the relative positions of sources that are sufficiently bright to be detected independently.

variability is one of the motivations for high-precision astrometry), and instrumental phase noise. Atmospheric limitations come in two forms: that due to the small-scale, rapidly varying structures that limit the coherence timescale, and that due to large-scale, slowly evolving features that induce anomalous phase delays resulting from the slighly different zenith angle, z, of the target and reference sources. As a result, the mitigation strategies for these differ substantially. Generally, we find that sub-beam precision is almost certainly achievable, with μ as accuracy likely possible. Note, however, that this accuracy is not always required. For example, the precision with which it is possible to register mm-VLBI and existing cm-VLBI images is necessarily limited by the resolution of the latter, which is roughly 0.1 mas.

As described in Appendix A, the short timescale of the rapid component implies that hundreds of realizations of the atmospheric turbulence are encountered in a typical observing night (roughly 2hr of on-source integration time). For phase references within 1.4° the atmospheric conditions will permit beamscale ($30\,\mu{\rm as}$) astrometry on $10\,{\rm s}$ intervals at $230\,{\rm GHz}$. Over $10\,{\rm min}$, the integration times used in Doeleman et al. (2009b) and Fish et al. (2011), this can be reduced to $4\,\mu{\rm as}$ scales. In a $2\,{\rm hr}$ period this may be reduced to $1\,\mu{\rm as}$. Thus, in practice, this is unlikely to be the dominant contribution to the astrometric uncertainty.

At 7 mm, the slowly varying, large-scale component dominates the astrometric uncertanties (Reid et al. 1999a), producing typical unmodeled time delays of 0.1 ns for sources separated by 1° in azimuth. This corresponds to an uncertainty on the order of 0.1 mas, i.e., three beam widths at 1.3 mm. However, there are a variety of schemes that may be employed to reduce this significantly. All of these seek to do so by exploiting the large spatial and temporal scales of the atmospheric fluctuations responsible for this component of the astrometric uncertainty.

The first is to implement better atmospheric models. The atmospheric model of Niell (1996) already accounts for the seasonal variations, generating daily estimates for the zenith phase delay, and thus does model the very-long timescale fluctuations. Improvements over this model come in a variety of forms, including the structure of the atmosphere assumed (Boehm et al. 2006a) and the inclusion of real-time weather modeling to produce accurate maps on 6hr timescales (Boehm et al. 2006b). These promise to reduce the size of the unmodeled phase perturbations by factors of a few.

The second is to periodically measure the group delays directly. This can be done using sets of known bright quasars, which are assumed not to move, so-called geodetic blocks, and has already been done in astrometric studies of the Galactic Center (Reid & Brunthaler 2004; Reid et al. 2009). Alternatively, this can be done using Global Positioning Systems (GPS) and Global Navigation Satellite Systems (GNSS) (see, e.g., Byun & Bar-Sever 2009). Already, GPS/GNSS is used to produce estimates for the zenith path delay with a time resolution of 5 min and precision of roughly 3 mm at sites comparable to those that will be employed by the EHT. This alone would be sufficient to improve the astrometric uncertainty due to the slow component by an order of magnitude, giving an accuracy of roughly $10\,\mu as$.

If three or more viable references are located in the vicinity of the target², a third strategy is to calibrate the unknown large-

scale phase delays directly. This can be done by asserting that the true positions of the references are fixed, and then using a procedure similar to that described in Appendix B to estimate the site specific phase delays by comparing the observed and expected reference separations (see also Fomalont 2005). This assumes that the references are not variable themselves, though even at μ as resolutions distant quasars are unlikely to exhibit structural variability on hour timescales. In principle, as shown in the appendix, the accuracy with which this can be done is comparable to the precision limit associated with the short-timescale variability, roughly $1\,\mu$ as.

Finally, the slow variations can be averaged down by combining observations over many days. The upper limit upon the time over which the observations can be combined is dictated by the time-scale of variations that are of interest. Thus, e.g., fluctuations in the position of Sgr A* on year-long timescales allows averaging over \sim 3 months, corresponding to $\sim 10^2$ independent realizations of the large-scale fluctuations, and thus a reduction in the uncertainty due to the slow-component of an additional order of magnitude.

In practice a combination of these mitigation strategies are likely to be required. Nevertheless, there is clearly a good reason to believe that μ as accuracies are achievable over long times via improved atmospheric modeling, direct phase delay measurement and time averaging. Furthermore, it may be possible to reach these accuracies over much shorter times using multiple phase references, though this is more speculative.

In the following sections we discuss some of the science made possible by phase-referenced mm-VLBI observations, and suggest possible phase references to be used for these purposes. Since many of the scientific motivations are different for Sgr A* and M87, the observing strategies also differ. Therefore, we address these sources separately.

3. SAGITTARIUS A*

Associated with the supermassive black hole located at the center of the Milky Way, Sgr A* is the primary target for the EHT. Presently, the best estimates of the mass (M) and distance (D) of Sgr A* come from the observations of orbiting stars (the so-called "S-stars"). These have yielded $M=4.3\pm0.5\times10^6M_{\odot}$ and $D=8.3\pm0.4$ kpc, respectively, where both include the systematic uncertainties (Ghez et al. 2008; Gillessen et al. 2009b,a). This results in an angular size for the apparent horizon of $53\pm2\,\mu{\rm as}^3$, the largest for any known black hole. The mass of Sgr A* is necessarily confined to within the periapse of nearby stars, giving a maximum radius of roughly $10^2\,{\rm AU}\simeq3\times10^3GM/c^2$.

3.1. Scientific Objectives

A variety of astrometric studies of Sgr A* have already been proposed and carried out. As a consequence of the large extinction towards the Galactic center, these necessarily are confined

are not subject to the same constraints that limit the reference-target separation. Since the distortion in the separation grows linearly with zenith separation, larger separations between reference sources result in larger relative phase perturbations due the large-scale fluctuations. However, the uncertainty associated with the rapid variations also grow nearly linearly, and thus the fractional precision with which the slowly-varying phase perturbations can be measured grows only slowly. Nevertheless, the number of bright references grows as separation squared. The separations are fundamentally limited by the region over which the large-scale atmospheric fluctuations can be accurately modeled.

³ Because the current mass and distance measurements are strongly correlated, with mass scaling roughly as $M \propto D^{1.8}$ (Ghez et al. 2008), the angular size of Sgr A* is constrianed much more strongly than M or D alone.

Note that because the atmospheric fluctuations that generate the slowly-varying phase perturbations are necessarily large, additional reference sources

to the radio and near-infrared (NIR). Nevertheless, a wide variety of objectives have been and are being pursued, including placing independent constraints upon the mass of the central supermassive black hole (Reid et al. 1999b; Reid & Brunthaler 2004, 2005) and detecting structural variations during radio and NIR flares (Reid et al. 2008; Bartko et al. 2009). A generic feature of these is the need for high astrometric precision. Here we describe how these efforts may be complemented or improved upon using the μ as precision afforded by mm-VLBI, as well as suggest additional scientific motivations for developing a mm-VLBI astrometry capability.

3.1.1. Constraints upon the Proper Motion of Sgr A*

The current hierarchical paradigm for black hole formation and active galactic nuclei (AGN) fueling is fundamentally dynamic, imparting large velocities to the central supermassive black holes. However, on timescales short in comparison to the time between galactic mergers this motion is dissipated by collective interactions between the supermassive black hole and the stars in the stellar bulge, i.e., dynamical friction (Chatterjee et al. 2002). Thus we expect the black hole at the center of the Milky Way to be nearly at rest, located at the bottom of the Galactic potential well. However, because of stochastic interactions with nearby stars, it will not be completely stationary and, if the surrounding stellar core is well described by a Plummer sphere, will execute random motions (perpendicular to the Galactic plane, say) with variance

$$\langle v_{\perp}^2 \rangle = \frac{2}{9} \frac{GM_{\text{tot}}}{a} \frac{m_{\star}}{M} \tag{1}$$

where M_{tot} is the total mass of the nuclear stellar cluster, m_{\star} is the characteristic mass of a star and a is the core radius of the Plummer sphere (Chatterjee et al. 2002; Reid & Brunthaler 2004). Thus, given an estimate of the stellar content within some radius, R, it is possible to constrain the the mass of Sgr A* given an upper limit upon its motion:

$$M > \frac{M_R}{1 + (9/2) \left\{ \langle v_{\perp}^2 \rangle a R^3 / \left[G \left(R^2 + a^2 \right)^{3/2} m_{\star} \right] \right\}},$$
 (2)

(Chatterjee et al. 2002; Reid & Brunthaler 2004). Note that this constraint is independent of those obtained from measurements of the orbits of stars immediately surrounding Sgr A*.

High-precision astrometric studies of Sgr A* have already been performed at 7mm using the Very Long Baseline Array (VLBA), constraining $\langle v_{\perp}^2 \rangle < 2 \, \mathrm{km s^{-1}}$, corresponding to $M > 2 \times 10^6 M_{\odot}$. They have also measured the apparent velocity parallel to the Galactic plane, giving $v_{\parallel} \simeq 250 \pm 16 \, \mathrm{km \, s^{-1}}$ (assuming a distance of 8.3 kpc to Sgr A*), which is presumably dominated by the contribution from the Sun's orbit in the Galaxy. The VLBA observations have a nominal astrometric precision of $10^2 \mu as$, and extend over a period of more than a decade. During this time they see no evidence for fluctuations, implying that either the motion is secular or has a period significantly exceeding $\sim 20 \, \text{yr}$. Note that the natural period for oscillations about the center of the average collective Galactic potential is dependent upon the radius (R_{inf}) of the region of influence, and roughly $7.4 \times 10^3 \left(R_{\rm inf} / 0.3 \, \rm pc \right)^{-3/2}$ yr, much larger than any observational period of interest.

Empirical estimates for the magnitude of the secular motion of Sgr A* are presently limited by the accuracy of individual radio observations. In principle, the uncertainty in the perpendicular component of the peculiar motion of the Sun provides

a fundamental limit upon efforts to measure the *secular* motion of Sgr A*. This is presently estimated to be $7.25\pm0.37\,\mathrm{km\,s^{-1}}$ relative to the local standard of rest (Schönrich et al. 2010). An additional uncertainty may arise from Galactic precession, which can be as high as $0.6\,\mathrm{km\,s^{-1}}$ in the extreme case in which the Milky Way "flips" in a Hubble time. These corresponds to an angular deviation of $9.4\,\mu\mathrm{as\,yr^{-1}}$ and $15\,\mu\mathrm{as\,yr^{-1}}$, respectively, both much smaller than the limits imposed by the accuracy of existing radio observations. Therefore, considerable improvement in the astrometric accuracy is possible in principle.

3.1.2. Detection of the Evolved Component of the Cusp

In addition to a secular component due the Sun's orbit and a potential displacement from the center of the Galactic potential, the velocity of the central supermassive black hole has a fluctuating component due to random forces applied by fluctuations in the surrounding retinue of stars and their compact remnants. In contrast to the secular motion, detecting a fluctuating component is made much simpler due to the variations in the velocity, which clearly differentiates it from contributions due to the solar motion. With μ as astrometric precision, detecting this fluctuating component on scales of a few years should be possible.

It is from this fluctuating component that the mass estimates described in the preceding section is ultimately derived. However, it is also possible to probe the spatial and mass distribution of the stars and their remnants in the immediate vicinity of Sgr A*. Understanding the properties of these objects is of intrinsic interest; how stars form and evolve in the Galactic center is presently poorly understood, characterized by the so-called "paradox of youth" (Ghez et al. 2003). However, it is also important as an exemplar. Detecting the stellar component would provide a direct means with which to estimate the rates of stellar disruptions and the subsequent contribution to the growth of AGN.

Furthermore, orbiting populations of stellar-mass black holes are expected to play a pivotal role in present and future gravitational wave searches. Stellar-mass black hole binary coalescence rates for the Laser Interferometer Gravitational Wave Observatory (LIGO) are strongly affected by the concentration of the stellar-mass black holes in galactic nuclei (O'Leary et al. 2009). Similarly, the event rate of extreme mass-ratio inspirals (EMRIs), one of the primary science drivers for the Laser Interferometer Space Antenna (LISA) (see, e.g. Miller et al. 2009; Schutz et al. 2009), is strongly dependent upon the density and mass function of stellar-mass black holes near the supermassive black hole (Sigurdsson & Rees 1997; Gair et al. 2004; Hopman & Alexander 2005, 2006; Gair et al. 2010; Amaro-Seoane & Preto 2010). We note that the environment of Sgr A* is particularly relevant to LISA, since it is comparable in mass to the systems that will dominate the LISA frequency band. In both cases, empirical estimates of the black hole distribution in Sgr A* can substantially reduce the uncertainties in the inferred merger rates.

Here we estimate the precision necessary to directly observe the motion induced upon Sgr A* by the nuclear stellar and black hole populations. To do this we assume a fiducial set of distributions for these objects, and consider both optimistic and pessimistic deviations from these. In all cases the natural frequency of oscillation about the minimum of the Galactic potential and the damping timescale due to dynamical friction with the stellar bulge (ω_0 and γ in Appendix C) are relevant

only at much larger timescales than the observationally motivated subset we consider (i.e., sub-century).

The stellar mass density surrounding Sgr A* has been inferred from infrared studies, finding that the total stellar mass density is well approximated by a broken power law:

$$\rho_{\star}(r) \simeq 1.7 \pm 0.8 \times 10^6 \left(\frac{r}{0.22 \,\mathrm{pc}}\right)^{-\gamma} M_{\odot} \,\mathrm{pc}^{-3} \,, \qquad (3)$$

where $\gamma = 1.2$ for $r < 0.22\,\mathrm{pc}$ and $\gamma = 1.75$ for $r > 0.22\,\mathrm{pc}$ (Schödel et al. 2007). This is well constrained observationally for $r > 10^{-2}$ pc, though there is considerable uncertainty regarding the structure of the core on smaller scales (Merritt 2010). In addition there is evidence for a preponderance of young stars in the vicinity of the supermassive black hole (Buchholz et al. 2009; Do et al. 2009, 2010). This biases the stellar mass function in the Galactic center towards higher masses. Nevertheless, here we make the conservative choice of adopting a stellar mass function indicative of the Galactic disk. Specifically, we employ the log-normal mass function for low-mass stars determined by Covey et al. (2008), smoothly joining a Salpeter high-mass tail, i.e., $\phi(m,r) \propto m^{-2.3}$ above $m \simeq 0.6 M_{\odot}$, and truncated at $10^2 M_{\odot}$. For our purposes here, it is enough to note that the average stellar mass and it's square are $m_{\star} = 0.75 M_{\odot}$ and $\mu_{\star}^2 \simeq 13.7 M_{\odot}^2$, respectively. Note that the Salpeter mass function immediately implies that $\mu_{\star}^2(r)$ is determined by the maximum mass and is generally much larger than m_{+}^{2} .

Less well constrained is the contribution from stellar remnants. Large numbers of stellar-mass black holes are expected to collect via dynamical friction in the vicinity of the central supermassive black hole (O'Leary et al. 2009; Alexander & Hopman 2009). A number of authors have estimated the number of stellar-mass black holes in the Galactic center, finding that roughly 2×10^4 are expected to exist within the inner pc (Morris 1993; Miralda-Escudé & Gould 2000; Hopman & Alexander 2006; Freitag et al. 2006; Alexander & Hopman 2009). The distribution of these remnants is less well understood; predictions ranging from flat cores to power-law cusps with indexes as extreme as -2.75 can be found in the literature (see, e.g., Alexander & Hopman 2009; Merritt 2010), though cusps with an indexes near -2 are most common. Thus we adopt a fiducial model for the black hole component given by

$$\rho_{\bullet} = \frac{m_{\bullet} N_{\rm pc}}{4\pi} \left(\frac{r}{\rm pc}\right)^{-2} M_{\odot} \,\mathrm{pc}^{-3}\,,\tag{4}$$

with $m_{\bullet} = 10 M_{\odot}$ and $N_{\rm pc}$ is the number of black holes in the inner pc.

In Appendix C we derive an approximate power spectrum for the displacement of the central supermassive black hole, $P_{x,\omega}$, for an arbitrary number density of objects, n(r), and a potentially radially dependent mass function, $\phi(m,r)$:

$$P_{x,\omega} \simeq \omega^{-4} \int_0^\infty dr \, \frac{2(2\pi)^{3/2}}{3} \frac{G^2 \mu^2}{r^2} \frac{n}{\Omega_k} e^{-\omega^2/2\Omega_k^2},$$
 (5)

with Ω_k given by Equation (C10). In this μ is the RMS mass at a given radius (thus weighted towards the more massive objects). At this point, there are some general features of note. First, since $P_{x,\omega}$ depends upon the object mass function through $\mu^2 n \sim \mu^2 \rho/m$ alone, when the same mass density is present, perhaps unsurprisingly, more massive stars/remnants result in proportionally larger displacements. Second, if μ^2 is fixed, $n(r) \propto r^{-\nu}$ with $\nu > 1/2$, and the motions of the stars/remnants

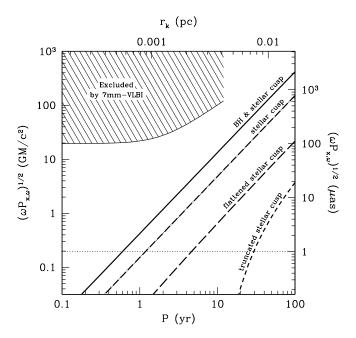


Figure 1. Characteristic displacements as a function of time-scale for when stellar mass black holes and stars are considered (solid), only the stellar component is considered (dot-dashed), when the stellar component is assumed to form a core of size 0.01 pc (long-dashed), and when all components are truncated inside of 0.01 pc (short-dashed). The region excluded by 7mm observations with the VLBA is shown by the hatched area (Reid & Brunthaler 2005). Along the left and right axes the displacements are shown in units of black hole mass and angle. Along the top axis the radius with Keplerian period equal to the time period is listed, providing some sense for the location of the objects that are dominating the fluctuations.

is dominated by the central supermassive black hole, we have

$$P_{x,\omega} \simeq \frac{2(2\pi)^{3/2}}{2\nu - 1} \frac{G^2 \mu^2}{r_{\min}} \frac{n_{\max}}{\Omega_{k \max}} \omega^{-4} \quad \text{for} \quad \omega < \Omega_{k,\max},$$
 (6)

i.e, $P_{x,\omega}$ is dominated by contributions from those objects nearest the central black hole and has a characteristic frequency dependence independent of the stellar distribution power law index. Thus, it is possible to make robust predictions for the scale of the jitter of Sgr A*, dependent primarily upon the maximum density and typical masses of stellar-mass objects in Sgr A*'s immediate vicinity.

Figure 1 shows the characteristic displacements, given by $\sqrt{\omega P_{x,\omega}}$, for a handful of possible stellar/remnant core models. In all but one the power spectrum follows it's asymptotic $\propto \omega^{-4}$ form (corresponding to $\omega^{-3/2}$ in the figure), despite the fact that n(r) is not a single power law and $\mu^2(r)$ ranges from $13.7\,M_\odot^2$ at large radii to $10^2\,M_\odot^2$ at small radii. What varies amongst the power spectra is primarily the normalization.

The solid line shows our most optimistic case, with the stellar and black hole components given by Equations (3) and (4), respectively, truncated at the innermost stable circular orbit (ISCO) of the central black hole, located at roughly 1.2×10^{-6} pc. In this case the displacement spectrum is dominated by the black hole component, and produces fluctuations in excess of a μ as on 0.5yr timescales. If, however, we ignore the remnant component altogether, the stellar component given by Equation (3) produces the dot-dashed line, implying that observable displacements will occur on 1yr timescales. In both cases the typical displacements on year-long timescales

are comparable to those estimated in Reid & Brunthaler (2004) (which find typical velocities of $0.3\,\mathrm{km\,s^{-1}}$ and $0.07\,\mathrm{km\,s^{-1}}$, producing angular displacements of $8\,\mu\mathrm{as}$ and $2\,\mu\mathrm{as}$ due to the remnant and stellar components, respectively⁴). This presumes that we are justified in extrapolating the observed stellar density all the way down to the ISCO, over four orders of magnitude. If instead we force the stellar density to saturate at 0.01 pc, the smallest scale for which the stellar distribution has been measured, we obtain the long-dashed line. Even in this case observable motions are present on sub-decade timescales. Finally, if we make the extreme pessimistic choice of truncating the stellar and black hole distributions at 0.01 pc we obtain the short-dashed spectrum, the curve of which is indicative of the lack of objects with sufficiently short periods to generate the short-timescale fluctuations.

3.1.3. Searching for a Massive Binary Companion

The hierarchical paradigm of galaxy formation also implies the presence of supermassive black hole binaries at the centers of some galaxies. Initially the supermassive black holes sink toward the center of the combined galaxy as a result of dynamical friction due to stars in the reassembled bulge and drag imparted by gas funneled into the galactic center by the merger. However, this process becomes inefficient when the binary separation shrinks to a few pc, at which point the stellar encounters that carry away the orbital angular momentum become rare. This is before gravitation radiation is able to drive the system to merger within a Hubble time, resulting in the so-called "final parsec" problem (Begelman et al. 1980; Roos 1981).

A number of solutions to the final parsec problem have been suggested, including triaxial bulges (Merritt & Poon 2004), massive perturbers (Perets & Alexander 2008), and interactions with the merger enhanced gas density (Escala et al. 2004, 2005). Nevertheless, in some fraction of systems long-lived supermassive black hole binaries are expected (Begelman et al. 1980; Yu & Tremaine 2003; Milosavljević & Merritt 2003; Gualandris & Merritt 2009). For this reason searches for supermassive binary companions have been performed in a variety of systems, primarily using spectroscopic methods (Bogdanović et al. 2009; Boroson & Lauer 2009; Decarli et al. 2010; Liu et al. 2010).

In the specific context of Sgr A*, massive companions and perturbers have been implicated for a very different reason: as a solution to the paradox of youth, i.e., the presence of the massive, and therefore young, stars orbiting Sgr A* (Ghez et al. 2003). Formation of the "S-stars" (typically B-type stars) in situ is thought to be precluded by the strong tidal forces from Sgr A*. This has lead to the development of models in which the stars are formed further out, where the restrictions are less severe, and then transported into Sgr A*'s vicinity (Gerhard 2001). However, it is only possible to reach the small radii observed if the S-stars were members of a very tightly bound cluster, requiring a heretofore undetected massive component, the prime candidate therefore being an intermediate mass black hole (McMillan & Portegies Zwart 2003; Hansen & Milosavljević 2003; Kim et al. 2004; Levin et al. 2005; Fujii et al. 2009; Merritt et al. 2009; Fujii et al. 2010). That is, the transport models imply the presence of a massive object located at a distance comparable to that of the S-star orbits, roughly 10^{-2} pc,

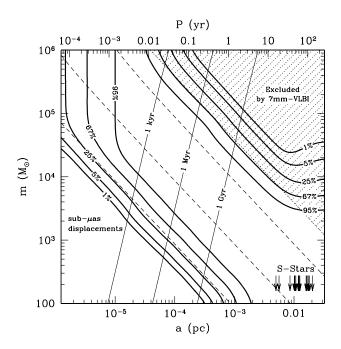


Figure 2. Non-excluded region of the companion mass—orbital separation parameter space that can be probed by astrometry with μ as precisions (cf. Hansen & Milosavljević 2003). Thick solid lines show (from outside in) locations in the parameter space with 1%, 5%, 25%, 67%, and 95% probabilities of not having been previously detected by previous astrometric studies at 7 mm with the VLBA (violated in the upper right) while exhibiting projected position shifts larger than a μ as at some point over the next decade (violated in the lower left). The dotted hatched area shows the approximate region described in the text that is ruled out by 7 mm VLBA studies. For reference, lines of constant maximum angular deviation are shown for circular orbits by the dashed lines, corresponding to $1\,\mu$ as (leftmost), $10\,\mu$ as, and $100\,\mu$ as (rightmost). Gravitational merger timescales for circular orbits are shown by the thin solid lines, ranging from 10^{-3} yr (leftmost) to 1 Gyr (rightmost). The period of the orbit (in the test particle limit) is shown along the top axis. Finally, the semi-major axes of the S-stars are indicated by the arrows.

from Sgr A*.

Thus, in addition to the stochastic buffeting from stellar-mass black holes and stars, Sgr A* may also move as a consequence of a massive binary companion. Whether or not this is observable astrometrically depends upon the orbital parameters, mass of the perturber and timescale of observations. Some set of these is already ruled out by the lack of an oscillatory signal in the 7 mm proper motion studies (Reid et al. 1999b; Reid & Brunthaler 2004, 2005). If we assume circular orbits with periods short in comparison to the observation time⁵, these rule out companion masses

$$m \gtrsim 8 \times 10^4 \left(\frac{a}{10^2 \,\text{AU}}\right)^{-1} M_{\odot} \,, \tag{7}$$

(see also Hansen & Milosavljević 2003). In the presence of eccentricity this expression is not a hard limit, since fortuitous orientations can result in small projected displacements.

Adopting a simple two-body model (i.e., ignoring the manybody effects of the stellar/remnant cusp) we estimate the likelihood of a given set of orbital parameters both satisfying the existing astrometric limits and executing deviations larger than

⁴ In Reid & Brunthaler (2004) the displacements due to remnants was twice as large as that reported here due to their assumption of twice as much mass in the black hole cusp.

⁵ For decade-long observations, this is true for $a \lesssim 0.01$ pc. Above 0.01 pc the orbital periods exceed 30 yr, and thus only a small fraction of the orbit would have been observed, decreasing the ability to probe these cases. Furthermore, at these distances the velocity is nearly constant, and thus degenerate with that due to the solar motion.

 $1 \,\mu$ as over the next decade. This provides some idea of the relevant parameter space that μ as-astrometry can exclude in the near future. Figure 2 shows this likelihood, marginalized over orbital orientation and eccentricity (assuming a flat prior) as a function of orbital separation and companion mass. As expected, large masses and orbital separations are already ruled out by Reid & Brunthaler (2005) (specifically, by requiring that the displacements be less than that observed perpendicular to the Galactic plane). While including eccentric orbits shift the location of this constraint. Equation (7) follows the contours of constant likelihood, falling nearly upon the 67% confidence level. At larger separations, the orbital period substantially exceeds the timescale over which the 7 mm VLBA observations of Sgr A* have been performed, and their diagnostic ability decreases. At small masses and orbital separations the companion induces only sub- μ as shifts in the position of Sgr A*, and is thus not likely to be detectable by the EHT. Even when the companion mass is sufficiently large, highly eccentric orbits pass within the ISCO, restricting the allowed parameter space further. Additionally, massive companions on small orbits merge rapidly, though an intermediate mass black hole associated with the S-stars would necessarily have entered the region in the past Myr. At large separations the fluctuations due to stellar-mass black holes described in Section 3.1.2 provide a source of additional noise (not shown in Figure 2). However, this is confined to the extreme lower right of Figure 2 even in the most optimistic cusp models. Regardless, for reference, the dashed lines in Figure 2 show the lower limits achievable with $1 \mu as$, $10 \mu as$, and $100 \mu as$ astrometric precision, assuming circular orbits. Thus, high-precision astrometry with the EHT should prove particularly effective for detecting massive companions to Sgr A*.

3.1.4. Imaging Dynamical Accretion/Ejection Features

The astrometric observations we have discussed thus far have focused upon detection of changes in the physical location of the supermassive black hole. However, astrometry is also sensitive to changes in the structure of the source. The observation of radio, NIR and X-ray flares in Sgr A*, with characteristic timescales ranging from ~ 20 min to hours, is strong evidence for substantial variability near the black hole horizon itself (Genzel et al. 2003; Eckart et al. 2006; Meyer et al. 2006; Porquet et al. 2008; Marrone et al. 2008). Highly variable, turbulent, magnetized plasmas flows are a generic component of both accretion and jet models for Sgr A*'s emission, and thus it is not surprising that transient features arise near the black hole with dynamical times comparable to the orbital timescale at the ISCO. Sgr A*'s flares are therefore naturally explained within the context of transient structural changes to the emitting region, e.g., orbiting hot spots generated by magnetic reconnection events or shocks and confined within a disk, expanding blobs of energetic material buoyantly ejected from a disk, or hot spots launched outwards in a jet. If this is indeed the case, flares should produce observable temporary fluctuations in Sgr A*'s location.

As new bright features emerge or move within the source the centroid of the image shifts, following the bright structures. The motion of the image centroid associated with orbiting hot spots, in the context of Sgr A*'s NIR flares, has been discussed at length (Broderick & Loeb 2005, 2006), and is the primary motivation for the GRAVITY instrument being developed for the Very Large Telescope Interferometer (see, e.g. Bartko et al. 2009). At 7 mm the opacity of the accretion flow precludes the observation of spots orbiting near the ISCO. Nevertheless, it

is possible to detect the motion associated with bright spots orbiting more than $30GM/c^2$ from the black hole using the VLBA (Reid et al. 2008). The EHT bridges the two regimes, and should access the innermost portions of the accretion flow with sufficient resolution to resolve any transient spots.

Detecting structural changes does not necessarily require absolute astrometry. If the image is not dominated by the dynamical feature, approaches based upon closure quantities and/or the evolution of the source polarization are capable of detecting changes in the shape and orientation of the emission region (Doeleman et al. 2009b; Fish et al. 2009). Alternatively, if the image uniformly brightens or expands, closure techniques can characterize the evolution of the emitting region. However, when a single transient feature dominates the emission, as has been observed to be the case for bright flares in the NIR, and this feature evolves structurally, absolute astrometry provides the only method to unambiguously detect the spatial variations.

More importantly, since the dynamical timescale in Sgr A* is ~ 10 min, the assumptions underlying Earth-rotation aperture synthesis are explicitly violated during flares. Specifically, we are no longer justified in assuming that the underlying source structure remains fixed throughout the night. For the EHT this is especially limiting; even when all existing and planned mm and sub-mm facilities are phased together, like the VLBA, the EHT will only be able to provide sparse instantaneous coverage of the u-v plane. With a sufficiently well specified model for the variability in hand, it is possible to analyze the visibilities directly, eliminating the need to produce images altogether. However, in the absence of such a model phase referencing provides the only means by which to relate visibilities at different times, producing approximate images of the time-averaged intensity.

Furthermore, in the presence of a single dominant spot, phase referencing may be required to remove the fundamental spot-disk degeneracy. That is, in the absence of an identifying feature that locates the black hole (e.g., the silhouette of the horizon, which may not be visible in the instantaneous images), fitting the self-calibrated visibilities alone will not be sufficient to distinguish a moving spot (either orbiting, infalling or outflowing) about a fixed quiescent disk and an artificially fixed spot with an artificially moving quiescent disk. Of course, absolute astrometry naturally resolves this ambiguity.

To address these issues, it is necessary to achieve sub-beam ($\lesssim 30 \,\mu as$) astrometric precision on the dynamical timescale of Sgr A* (~ 20 min). As long as a sufficiently strong phase reference is within $\sim 1^{\circ}$, this should be possible with the EHT.

3.2. Possible Phase References

Phase reference candidates must satisfy a number of constraints. Chief among these are brightness and compactness; the reference must be detectable in mm-VLBI observations. Most of what we describe in this section are efforts to characterize these properties. However, in addition the structure of the phase reference and Sgr A* must be stationary over the timescale of the experiment. In the case of the latter this is assisted by direct imaging, which can unambiguously identify the location of the black hole via it's silhouette against the nearby emitting material. For the phase references the case for stability is less clear, and ultimately, this will have to be empirically established. Here we will assume that this can be done. For quasars this is well justified, being located at extraordinary distances. For masers this may not be, limiting their utility to short-term (days or weeks) uses only. Using multiple phase references provides a means to test this assumption and potentially mitigate violations.

3.2.1. Quasars

The quasars J1745-282 (W56), J1748-291 (W109), and J1740-293 (GC 441) are located within 1° of Sgr A*, and have been used previously as phase references for proper motion studies of Sgr A* with the VLA (Backer & Sramek 1999). The first two have been successfully used in VLBI observations at wavelengths of 3.5 cm and above (Reid et al. 1999b; Bower et al. 2001; Reid & Brunthaler 2004). We show the spectral energy densities (SEDs) of these sources are in Figure 3. These are constructed from the literature and are therefore not contemporaneous, varying over nearly 30 years (Isaacman et al. 1980; Zoonematkermani et al. 1990; Bower et al. 1999, 2001, 2002; Nord et al. 2004; Roy et al. 2005). As a consequence, the uncertainties reflect the larger of either that associated with the intrinsic measurement or that due to the variability implied by the multi-epoch observations.

All of these are optically thin above 43 GHz. At frequencies above this transition we assume the SED is characterized by a power-law, which we extrapolate to obtain single-dish flux densities at 230 GHz and 345 GHz. Inferring the magnitudes of visibilities on long baselines then requires some assumption about the source structure; here we make the extreme simplifying assumption that the candidate references are point sources. Therefore, we compare the extrapolated flux densities directly to those presented in Table 1. However, these may be considerable overestimates if substantial structure is not present on scales smaller than $\sim 10^2 \,\mu as$ in these objects. While the point source approximation may not be justified (e.g., the flat highfrequency spectrum of J1745-282 suggests the presence of a compact optically thick component, and thus extended structure), the observed sizes of the candidate references at longer wavelengths are consistent with those of point sources, scatter broadened by the intervening interstellar electrons ⁶.

The steep spectrum of J1740-293, shown in the bottom panel of Figure 3, predicts fluxes well below the limits along any baseline at both 230 GHz and 345 GHz. This is unsurprising since J1740-293 is already too dim at 43 GHz to be employed as a phase reference (Reid et al. 1999a). Thus, while we include it here for completeness, it is almost certainly excluded as a potential phase references at shorter wavelengths as well. By comparison, both J1748-291 and J1745-282 are used as phase references for proper motion studies of Sgr A* (Reid et al. 1999a; Reid & Brunthaler 2004; Reid et al. 2008).

J1748-291 transitions into the optically thin regime between 1.4 GHz and 8.4 GHz, above which the SED appears well characterized by a power-law. As seen in the middle panel of Figure 3, there is some uncertainty in the mm flux densities, deriving from the considerable uncertainty in the 22 GHz and 43 GHz fluxes. This arises in part due to the lower resolution of the VLA observations at 8.4 GHz in comparison to the VLBA measurements at higher frequencies. While these agree within their respective uncertainties, including only VLBA data points produces a flatter spectrum on average, and thus higher mm flux densities. Nevertheless, it is clear that J1748-291 is unlikely to be sufficiently bright to be used as a phase reference by the EHT-I. For the EHT-C, it is still too dim to be detected on the

Hawaii–CARMA baseline, though may achieve marginal detections on baselines including more than 10 ALMA antenna. For this reason we consider J1748-291 to be a marginal case.

In contrast, J1745-282 is almost certainly bright enough to be used as a phase reference at 230 GHz for both the EHT-I and EHT-C, and 345 GHz in the case of the latter. The spectral index of J1745-282 is poorly constrained at present since the SED transitions to the optically thin regime near or above 8.4GHz. More importantly, the 43 GHz flux estimates are limited by atmospheric transmission effects, which bias the estimates towards lower values. As a result, the highest observed flux values may be better estimates of the high-frequency luminosity of J1745-282 than the average value. Therefore, in the interest of completeness we show both, and their associated estimates, in the left panel of Figure 3. In the former case the spectrum remains inverted at high frequencies, implying flux densities of $\sim 0.1 \, \text{Jy}$ at mm wavelengths, well in excess of the various detection limits. In the latter case, the flux densities are more modest, $\sim 30 \,\mathrm{mJy}$, and comparable to the limits for the EHT-I. Nevertheless, both estimates imply that for the EHT-C J1745-282 is a strong mm-VLBI phase reference candidate.

3.2.2. Masers

Masers provide an attractive alternative due to their small intrinsic size and large brightness temperature. Many molecular transitions exist that can produce masers at high frequencies, and those at mm and sub-mm wavelengths have only begun to be investigated (Humphreys 2007). Known sites of maser emission in the Galactic center include AGB stars (e.g., IRS 7, Menten et al. 1997; Reid et al. 2003, 2007) and nearby star formation regions (e.g., Sgr B2, Qin et al. 2008; Reid et al. 2009; Caswell et al. 2010).

The SiO masers associated with AGB stars are believed to originate within 4–5 stellar radii ($\sim 8\,\text{AU}$) of the star itself. However, typical AGB stellar radii are $\sim 300R_{\odot}$, implying an angular scale for the masing region of roughly 1 mas (Reid & Menten 2007). As a consequences, many of these sources will almost certainly be resolved out by mm-VLBI observations, eliminating them as candidate phase references.

In contrast, H₂O masers have been observed to have typical extents comparable to an AU within star forming regions, corresponding to an angular scale $\sim 10^2 \, \mu \mathrm{as}$ (Reid & Moran 1981), and H₂O maser spots an order of magnitude smaller have been observed surrounding late-type stars (Imai et al. 1997). At 22 GHz, H₂O masers have already been used in VLBI astrometry observations within the Galactic center. Reid et al. (2009) report the detection of a number of strong maser sources in the Sgr B2 complex with typical sizes of ~ 0.3 mas. This is much smaller than the $\sim 2\,\mathrm{mas}$ scatter-broadened size of a point source co-located with Sgr A* at 22 GHz, and thus it is unclear how much of the observed typical maser spot size arises due to interstellar electron scattering. As a consequence the Sgr B2 maser spot observations may be consistent with much smaller intrinsic sizes. High-frequency H₂O maser transitions at 325 GHz and 380 GHz have been observed with fluxes similar to that of associated 22 GHz H₂O masers surrounding late-type stars.

As with quasars, the need to detect the masing region within the atmospheric coherence time produces a flux limit, below which the maser is not a viable phase reference candidate. Unlike continuum sources, however, the line-like nature of the maser prevents the EHT from leveraging large bandwidths to increase sensitivity. Rather, the signal-to-noise ratio is maximized when the observing bandwidth matches the maser line

 $^{^6}$ The interstellar electron scattering that broadens images of the Galactic Center is subdominant at mm wavelengths. Since the size of the scattering kernel, well described by an asymmetric gaussian, scales as λ^2 , this is not true at longer wavelengths, where scattering necessarily induces correlated flux losses.

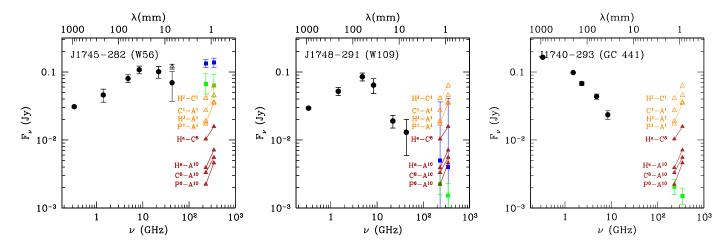


Figure 3. SEDs of radio-bright quasars within 1° of Sgr A* considered by Bower et al. (2001). The flux densities shown by the black circles were taken from the literature and are not contemporaneous (Isaacman et al. 1980; Zoonematkermani et al. 1990; Bower et al. 1999, 2001, 2002; Nord et al. 2004; Roy et al. 2005). Thus the error bars indicate the larger of the intrinsic measurement uncertainty or the variability amongst multiple data points at a given frequency. Green squares show the inferred flux densities at 230 GHz and 345 GHz. For J1745-282 the 43 GHz flux measurement is highly variable, due presumably to observing conditions, and thus we also show the inferred high-frequency flux densities associated with the brightest 43 GHz measurement by the blue squares. For J1748-291 the blue squares show the mm flux densities inferred from VLBA observations alone. For reference the sensitivities of baselines consisting of stations with multiple telescopes at both ends are shown at 230 GHz and 345 GHz, by the open-orange and filled-red triangles (see the text for details).

width, which for typical velocity widths of $\Delta V \sim 5\,\mathrm{km\,s^{-1}}$ are roughly 4MHz at 233GHz. The corresponding detection threshold is then dependent upon the velocity width, with

$$F_{\nu}^{M} = F_{\nu,0}^{M} \left(\frac{\Delta V}{5 \,\mathrm{km} \,\mathrm{s}^{-1}} \right)^{-1/2} \tag{8}$$

for which the coefficients $F_{\nu,0}^M$ are given in Table 1. These are typically on the order of 1 Jy for the EHT-I and 0.3 Jy for the EHT-C. By comparison, these are much smaller than the typical flux of 40 Jy reported for the Sgr B2M spot observed at 22 GHz by Reid et al. (2009).

4. M87

M87 is well known as a prototypical AGN, exhibiting a powerful relativistic jet. Recent analyses of its surrounding bulge have produced mass and distance estimates for the central supermassive black hole of $6.6 \pm 0.4 \times 10^9 M_{\odot}$ and 17.9 Mpc, respectively (Gebhardt & Thomas 2009; Gebhardt et al. 2011). As a consequence, the angular size of M87's horizon is roughly 70% that of Sgr A*'s, and thus M87 is an excellent second target for the EHT.

4.1. Scientific Objectives

The scientific objectives that can be addressed with shortwavelength astrometric observations in M87 are qualitatively different from those described for Sgr A* for two reasons. First, M87's much larger mass results in correspondingly substantially larger dynamical scales. Unlike Sgr A*, M87 evolves slowly, with the period at the ISCO of \gtrsim 5 days, and thus using Earth-rotation aperture synthesis is well justified even for epochs of large variability. Similarly the time and mass scales for massive companions are increased by $\sim 1.5 \times 10^3$. Thus, decade long observations can only search for objects within $\sim 1.4 \times 10^2 GM/c^2$, and more massive than $\sim 10^7 M_{\odot}$. However, such a supermassive black hole binary will merge in less than 5 Myr due to gravitational radiation alone, and is thus exceedingly unlikely. Finally, fluctuations in M87's position driven by stellar-mass black holes are essentially undetectable

as a result of both, the increased timescale and the much larger mass of the central object.

Second, in contrast to Sgr A*, M87 powers an ultrarelativistic jet. For this reason M87 has already been subject of a number of high-resolution imaging efforts (Junor et al. 1999; Ly et al. 2004; Krichbaum et al. 2006; Kovalev et al. 2007; Ly et al. 2007; Walker et al. 2008). Nevertheless, the relationship between the observed jet emission and the black hole remains unclear (see, e.g. Marscher et al. 2008). By resolving the horizon, the EHT will unambiguously identify the central black hole. Registering the mm/sub-mm and radio VLBI images will therefore allow the conclusive determination of the location of the black hole relative to the larger-scale radio features. Note that to achieve this, μ as precision is not required; the ability to position the radio VLBI and mm/sub-mm images is fundamentally limited by the astrometric precision at longer wavelengths, roughly $30 \,\mu as$. Positioning the black hole in this manner provides immediate insight into a variety of aspects of the relationship between the central supermassive black hole and the surrounding larger-scale emission, with associated implications for jet formation. In the remainder of this section we expand upon what can be learned by relating the mm and radio images.

4.1.1. Locating the Counter Jet with Implications for Inclination and Acceleration

Ly et al. (2007) and Kovalev et al. (2007) report tantalizing evidence for the presence of a counter jet in M87. This arises from stacking multiple self-calibrated images, though it is probably not a calibration artifact. However, the interpretation of this feature as a counter jet hinges upon the identification of the core as the black hole location. In the absence of phase referenced VLBA observations of M87 showing symmetric outflowing motions, this remains an assumption.

The presence of a counter jet places severe constraints upon the inclination angle, Θ , and acceleration of M87's jet. Making the simplifying assumptions that the jet and counter jet are symmetric, with constant spectral indexes ($S_{\nu} \propto \nu^{-\alpha}$), and only moving radially with Lorentz factor Γ , the observed brightness

ratio is approximately

$$R_B \equiv \frac{I_J}{I_{CJ}} \simeq \left(\frac{1 + \beta \cos\Theta}{1 - \beta \cos\Theta}\right)^{\alpha+2} \simeq \left(\frac{4}{\Gamma^{-2} + \Theta^2}\right)^{\alpha+2},$$
 (9)

where in the final expression the empirically well-justified approximations $\Gamma\gg 1$ and $\Theta\ll 1$ were made. Note that this is a function of distance from the jet and in general will not be constant near the black hole.

For large Lorentz factors, and thus at large distances, R_B , is a function of Θ alone. The observed brightness ratio for the putative counter jet is ~ 15 , and is roughly consistent with the inclinations of 30° – 45° obtained by radio proper motion studies (Reid et al. 1989; Ly et al. 2007). This is, however, much larger than the 20° upper limit implied by apparent motions of $\sim 6c$ found by optical proper motion studies (Biretta et al. 1999). There are many possible explanations for this discrepancy, including asymmetric jets, anisotropic emission, significant toroidal velocity components, significant jet structure and variable spectral indexes, as well as the misidentification of the counter jet.

Near the black hole, within the jet acceleration region Γ can be considerably smaller than the asymptotic value at large distances. This is consistent with radio observations of moving features, finding proper motions up to 2c within 2 mas from the core (Walker et al. 2008), in contrast to the fast moving optical features 500 times further away. When $\Gamma \lesssim \Theta^{-1}$, R_B becomes a rapidly varying function of distance from the core, providing an independent means to estimate the acceleration of the bulk flow within the jet as a function of radius.

Utilizing the counter jet to study the jet acceleration and orientation is necessarily predicated upon an accurate determination of the location of the central supermassive black hole for two reasons. First, robustly identifying a given image feature as being due to the counter jet is done most naturally by relating its position to that of the black hole and jet. Second, since the jet brightness evolves as it moves away from the launching region, quantitatively comparing the jet—counter jet brightnesses even for the idealized, symmetric case, requires accurate distances from the central black hole. Positioning the supermassive black hole within the core via EHT observations would remove any ambiguity regarding the black hole location, and would undergird the interpretation of the putative counter jet.

4.1.2. Unambiguous Measurement of the Jet Opening Angle

AGN jets are known to have remarkably small opening angles on large scales. This is set by both, the size of the jet launching region and the rapidity with which the jet is collimated. For M87, 7 mm images exhibit a radio core and a jet containing two limb-brightened features, with opening angle 15°, commonly associated with the opening angle of the jet itself (Junor et al. 1999; Ly et al. 2004; Krichbaum et al. 2006; Kovalev et al. 2007; Ly et al. 2007; Walker et al. 2008). However, these limb-brightened features do not appear to converge upon the 7 mm core, intersecting roughly 2 mas east of it (Ly et al. 2007). One is then driven to one of three possible conclusions, depending upon the location of the black hole and the breadth of the jet launching region.

First, the 7 mm core does not indicate the position of the central black hole, and is instead a feature within the inner jet, e.g., as suggested by Marscher et al. (2008). In this case, it isn't clear why the region surrounding the black hole doesn't radiate. Nevertheless, the 7 mm jet morphology would be broadly consistent with jet formation theory.

Second, the 7 mm core does indicate the position of the central black hole, and the jet rapidly collimates, begining from exceedingly large opening angles ($\gtrsim 60^\circ$) and reaching its asymptotic conical structure within $\sim 0.3 {\rm mas} \simeq 10^2 GM/c^2$ of the black hole (Junor et al. 1999). When the inclination exceeds the largest opening angle, projection of the jet on the plane of the sky significantly enlarges the apparent opening angle further, though this is insufficient to explain the rapid evolution in the opening angle by itself. In this case, M87 presents a serious challenge to many jet formation theories, and jet formation simulations in particular.

Third, the 7 mm core does indicate the position of the central black hole, and the 7 mm jet seen on mas scales is associated with a different structure than the optical jet seen at large distances. This would naturally account for the systematically lower velocities observed in the radio images. In this case the transrelativistic unbound wind seen in many jet formation simulations is a natural candidate for the structure responsible for the 7 mm jet feature.

Locating the black hole with the EHT, and translating that location to the longer-wavelength radio images, conclusively addresses the distinction between the first two: either the black hole is located in the radio core or not. Furthermore, since the EHT promises to resolve the jet launching region, it will be capable of distinguishing between the compact ultrarelativistic jets and broad trans-relativistic winds (Broderick & Loeb 2009). By registering the mm-VLBI image to the longer-wavelength VLBA images, the relationship between the anticipated components of the outflow and the larger-scale features of the radio images may be determined.

4.1.3. Identifying the Source of Jet Variability

M87 is known to be variable on timescales of weeks, generating bright knots which rapidly propagate away from the radio core. The apparent speeds of these knots vary considerably, ranging between 0.2c to 2.5c (Ly et al. 2007; Kovalev et al. 2007; Walker et al. 2008). In at least one case these have been accompanied by a TeV flare (Acciari et al. 2009; Wagner et al. 2009), implying that the source of the variability lies close to the black hole. However, where the variability originates remains to be determined. Possible sources include variations in the accretion rate, turbulence within the accretion flow, and instabilities within the jet itself (see, e.g., Giannios et al. 2010). Monitoring M87 with coincident phase-referenced EHT and VLBA observations allows variable features to be followed from horizon to parsec scales. Those arising near the black hole will be clearly identifiable by their proximity to the silhouetted horizon.

4.2. Possible Phase References

Located well out of the Galactic plane, M87 does not suffer the interstellar electron scatter-broadening and extinction associated with studies of the Galactic center. This has facilitated the identification of a number of compact sources within it's vicinity. However, few of these are radio sources, and fewer still have been studied at VLBI resolutions. As a consequence, the primary uncertainty associated with the viability of potential mm-VLBI phase references for M87 is their compactness. Nevertheless, we have identified a number of possible targets, which we list in order of decreasing viability.

Located 1.52° away from M87, M84 (NGC 4374) is one of the few sources near M87 for which it is possible to find multiple VLBI observations in the literature. As with many of the

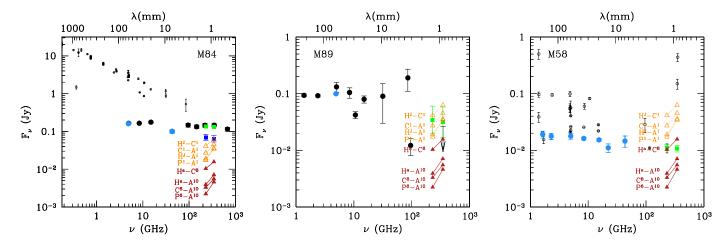


Figure 4. SEDs of bright radio sources within 2° of M87, obtained from the literature. Left: SED of M84. The flux densities shown by the large filled circles correspond to observations with beam FWHMs smaller than 35". Those shown in blue are VLBI observations, with typical beam sizes of mas. The 230 *GHz* and 345 GHz fluxes implied by all of these points and the VLBI points alone are shown by the green and blue squares (respectively). The small circles show all of the radio flux densities in the NED and VizieR databases associated with beams larger than 35", and are presumably indicative of the galactic non-thermal emission. Middle: SED of M89. Large light blue circles show VLBI observations, while large black circles show all other radio observations in the NED and VizieR databases. The green squares correspond to the 230 GHz and 345 GHz flux densities implied by all observations. For comparison, an upper limit at 347 GHz is shown by the arrow. Right: SED of M58. Large light blue circles show VLBI observations, while small open circles show all other radio observations in the NED and VizieR databases. The green squares are the 230 GHz and 345 GHz flux densities implied by the VLBI measurements. In all panels, for reference the sensitivities of baselines consisting of stations with multiple telescopes at both ends are shown at 230 GHz, by the open-orange and filled-red triangles (see the text for details).

phase references we consider here, separating the contributions to the SED, shown in Figure 4, associated with the surrounding galaxy and the compact core is the primary difficulty. In the case of M84 we do this via the resolution dependence of the spectral index. The SED obtained from observations found via NED⁷ and VizieR (Ochsenbein et al. 2000) with large beams (FWHMs > 35", small open circles, Heeschen & Wade 1964; Pilkington & Scott 1965; Pauliny-Toth et al. 1966; Gower et al. 1967; Ekers 1969; Kellermann et al. 1969; Stull 1971; Witzel et al. 1971; Pauliny-Toth & Kellermann 1972; Slee & Higgins 1973; Kellermann & Pauliny-Toth 1973; Condon & Jauncey 1974; Heeschen & Conklin 1975; Sramek 1975; Wills 1975; Genzel et al. 1976; Véron 1977; Pauliny-Toth et al. 1978; Dressel & Condon 1978; Geldzahler & Witzel 1981; Large et al. 1981; Kuehr et al. 1981; Bennett et al. 1986; Becker et al. 1991; Gregory & Condon 1991; White & Becker 1992; Slee 1995; Douglas et al. 1996; Condon et al. 2002; Vollmer et al. 2004; Cohen et al. 2007) shows a characteristic steep powerlaw, almost certainly associated with the galactic synchrotron component. In contrast, the SED associated with observations with small beams (FWHMs < 35", large filled circles, Leeuw et al. 2000; Nagar et al. 2001, 2002; Leeuw et al. 2004; Ly et al. 2004; Doi et al. 2005; Nagar et al. 2005), and VLBI observations in particular (FWHMs \sim mas, large filled blue circles, Ly et al. 2004; Nagar et al. 2005), exhibit the flat spectrum indicative of AGN, extending from 5 GHz (the smallest frequency at which sufficiently small beam observations have been performed) to 670 GHz, above which dust emission begins to dominate (Leeuw et al. 2000, 2004; Doi et al. 2005). Below 43 GHz the small-beam and VLBI flux densities are similar, implying that in the radio, the small-beam observations are dominated by the emission on sub-mas scales. At far-infrared wavelengths, Doi et al. (2005) have excluded other potential sources of contamination (galactic synchrotron, free-free and dust emission), arguing that the dominant component is also due to the AGN itself. As a result, the existing 0.85 mm (350 GHz) and 1.35 mm (221 GHz) flux measurements, obtained via the JCMT with sub-20" beams, provide a plausible estimate for the 230 GHz and 345 GHz fluxes that will be observed by the EHT; finding values in excess of 0.1 Jy (green-squares). Nevertheless, we also extrapolate flux estimates from the VLBI observations alone, finding estimates on the order of 0.07 Jy. In both cases these are considerably larger than the flux limits of the EHT-C at 230 GHz. For the EHT-I, M84 is still almost certainly sufficiently bright to be used as a phase reference at 230 GHz, and is marginal at 345 GHz. As a result, M84 is likely to be a strong mm-VLBI phase reference candidate.

M89 is somewhat closer to M87, at an angular separation of roughly 1.19°. The radio SED of M89 is shown in Figure 4, in which all of the data points were taken from the literature (Heeschen & Conklin 1975; Sramek 1975; Dressel & Condon 1978; Becker et al. 1991; Gregory & Condon 1991; Nagar et al. 2001; Condon et al. 2002; Filho et al. 2004; Vollmer et al. 2004; Doi et al. 2005; Nagar et al. 2005; Healey et al. 2007; Braun et al. 2007) As with M84, there is a paucity of VLBI observations, in this case only the one by Nagar et al. (2005), though the resulting core flux density is similar to VLA observations at the same frequency, differing by roughly 30% (cf. Becker et al. 1991; Gregory & Condon 1991; Sramek 1975; Nagar et al. 2001). This again suggests that the lower-resolution observations are dominated by the compact core. Unlike M84, there is a substantial scatter in the high-frequency ($\sim 90\,\mathrm{GHz}$) flux densities, possibly due to resolution, an interpretation supported by the fact that the relevant beam widths varied by an order of magnitude, with the smaller beam measuring the smaller flux density (e.g., Heeschen & Conklin 1975; Doi et al. 2005). This is unlikely to be responsible for the scatter at lower frequencies (near 10 GHz), where the higher-resolution observations produce higher flux density estimates, though during a different epoch (e.g., Nagar et al. 2001; Vollmer et al. 2004). Therefore, to infer the 230 GHz and 345 GHz flux densities we fit a single power-law to all of the M89 radio data. This results in values that are consistent with the 347 GHz upper limit obtained by

⁷ The NASA/IPAC Extragalactic Database (NED) is operated by the Jet Propulsion Laboratory, California Institute of Technology, under contract with the National Aeronautics and Space Administration.

Doi et al. (2005); sufficiently bright for the EHT-C, and only marginal for the EHT-I. Thus, we also consider this a strong candidate mm-VLBI phase reference candidate, though clearly less so than M84.

The final candidate we show in Figure 4 is M58, again with the radio SED obtained from the literature (Heeschen & Wade 1964; Sramek 1975; Dressel & Condon 1978; Gregory & Condon 1991; Becker et al. 1991; White et al. 1997; Nagar et al. 2001; Ulvestad & Ho 2001; Condon et al. 2002; Vollmer et al. 2004: Anderson et al. 2004: Nagar et al. 2005: Dale et al. 2005: Doi et al. 2005; Gallimore et al. 2006; Krips et al. 2007). Separated by 1.78° from M87, M58 is the further than M84 and M89, though still well within the isoplanatic angles at the relevant EHT stations on good nights. Unlike M84 and M89, sufficient VLBI observations exist for M58 to completely characterize its radio spectrum, from 1.7 GHz through 43 GHz (Anderson et al. 2004; Nagar et al. 2005; Krips et al. 2007). These allow a reasonably precise estimate of the mm-VLBI flux densities, giving values comparable to the sensitivity limits of the EHT-C at 230GHz, and well below them along the Hawaii– CARMA baseline at 345 GHz. As a consequence, this is a marginal phase reference candidate.

There are a number of additional bright sources near M87, though none are well studied at sufficiently high resolutions to make definitive statements regarding their millimeter fluxes on sub-mas scales. Within 1°, the most promising candidates are J1229+114 (PKS 1227+119, VPCX 27) and J1230+114 (VPCX 28). Extrapolating from the existing radio data (Shimmins et al. 1975; Large et al. 1981; Wright & Otrupcek 1990; Becker et al. 1991; White & Becker 1992; Ledlow & Owen 1995; Gregory et al. 1996; White et al. 1997; Laurent-Muehleisen et al. 1997; Condon et al. 1998; Reich et al. 2000; Cohen et al. 2007) gives estimates for the millimeter fluxes comparable to, or in excess of, the detection limits of the EHT-C, though in most cases comparable to the limits for the EHT-I. However, these conclusions are contingent upon a substantial fraction of the radio flux arising from sub-mas scales. There is some evidence for the radio emission in J1229+114 being primarily associated with the AGN, as opposed to galactic synchrotron; J1229+114 has been classified as an FRI based upon the 1.4 GHz morphology as measured at 5" resolutions by the FIRST survey, performed with the Very Large Array (White et al. 1997; Gendre & Wall 2008). However, at 5" it is already apparent that the source is extended, with the unresolved core constituting approximately 10% of the overall flux (White et al. 1997). Similarly, Flesch (2010) assigns a 41% probability that J1230+114 is associated with a quasar based upon radio-X-ray associations. Furthermore, it is the only radio source within 5' of MC2 1227+120, classified as a quasar in Veron-Cetty & Veron (1983), despite the lack of this source in the Molongo catalogs (cf. Large et al. 1981). Nevertheless, since neither object has been observed with resolutions exceeding 5", whether or not J1229+114 and J1230+114 are suitable phase references remains highly uncertain.

Finally, many of the science objectives described in Section 4.1 require only registering the mm-VLBI and cm-VLBI reference frames. As a consequence, many of these can be achieved with astrometric accuracies of $\sim 0.1\,\mathrm{mas}$. Furthermore, due to the long dynamical timescale of M87, it is possible to combine observations over many nights to reduce the astrometric error. However, as shown in Appendix A, the constraint upon the proximity of the phase reference is dependent upon the astrometric precision desired and the length of the observation. Specifically, Equation A12 implies that 0.1 mas pre-

cisions may be achieved at all relevant EHT stations over the course of a single night, corresponding to hundreds of independent 10 s measurements, for $\delta \lesssim 20^{\circ}$. While this is sufficiently large that it violates some of the assumptions made in deriving Equation A12, it is nevertheless clear that angular separations much larger than a few degrees are permissible for this purpose. Thus, we include a fifth possible reference, the wellstudied bright quasar 3C 273, located 10.3° away from M87. A sufficient number of VLBI flux measurements exist for 3C 273 to produce an SED from these alone (Krichbaum et al. 1997: Lonsdale et al. 1998; Kellermann et al. 2004; Zavala & Taylor 2004; Horiuchi et al. 2004; Lister & Homan 2005; Kovalev et al. 2005; Cara & Lister 2008; Lee et al. 2008). They include the observation by Krichbaum et al. (1997) at 215 GHz which found a flux density of 9.2 ± 0.6 Jy. As a result, there is no question that 3C 273 is bright enough at millimeter and submillimeter wavelengths to be used as an astrometric reference.

5. CONCLUSIONS

The EHT promises to usher in an era of μ as black hole astronomy. This takes the form first of $\sim 20\,\mu$ as-resolution images, allowing careful study of the morphology and dynamics of accretion flows and jet formation on sub-horizon scales for a handful of supermassive black holes, including Sgr A* and M87. Because these images resolve the horizon, they unambiguously locate the black hole via its silhouette against nearby emission. However, it also allows high-precision astrometric observations, relating the positions of Sgr A* and M87 to nearby, bright, compact sources. This is only possible because many of the EHT VLBI stations are arrays, allowing coincident observations of the source and a reference without having to repoint the antennas on the atmospheric coherence time, roughly $10\,s$. On a typical night, atmospheric turbulence limits the precision to $4\,\mu$ as over $10\,$ min and $1\,\mu$ as over many hours.

Necessary for μ as-precision astrometry with the EHT is nearby, bright point sources. This is complicated by both the short wavelength (few objects are bright in the mm) and the very high angular resolution of the EHT (many objects are resolved out). Nevertheless, with the anticipated 4 GHz bandwidths a variety of sufficiently bright possible phase references exist near Sgr A* and M87. While in most cases we cannot determine the mm-size of these objects, in all cases they have not been resolved out at 7 mm. Note that we have concerned ourselves solely with objects that can be detected individually on timescales shorter than the atmospheric coherence time, and thus the sensitivity/brightness limits can be relaxed if these objects are phase referenced by the primary source (e.g., Sgr A* or M87).

The kinds of science that μ as-precision astrometry enables depends critically upon the object under consideration. Many of the processes that potentially affect the position of the central, supermassive black hole depend upon its mass, while the questions of interest depend upon its environment. In all cases, however, the unique ability of mm-VLBI to conclusively locate the position of the supermassive black hole is used.

Sgr A* is constantly buffeted by objects within the evolved stellar cusp. Even with extremely pessimistic assumptions regarding the content and structure of the cusp, over year timescales, this produces μ as displacements in Sgr A*'s position. While the presence of these displacements is robust, the magnitude is sensitive to the properties and density of the objects within the cusp, and thus provides a means to probe these. Detection of the expected stellar-mass black hole cusp would

have far reaching implications for the event rates of existing and future gravitational wave searches.

Sgr A* is also potentially perturbed by massive binary companions. Frequently invoked to explain the presence of young, massive stars within 10^2 AU of Sgr A*, an intermediate black hole orbiting Sgr A* has an infall timescale (dominated by gravitational radiation) that is long in comparison to the lifetimes of the young stars. If such a binary exists it will induce periodic displacements in Sgr A*'s position, the size of which depend upon the object's mass and orbital parameters. While some portion of the available parameter space has previously been excluded by 7 mm astrometric studies, the μ as-precision astrometry made possible with the EHT is capable of eliminating the vast majority of the remaining parameters with subdecade observations.

Efforts to image Sgr A* must necessarily contend with its sub-hour, large-amplitude variability. This formally precludes Earth aperture synthesis, which assumes that the source is fixed throughout the night and is not amenable to self-calibration techniques, which smear dynamic images in an ill-defined fashion. Phase reference observations provide a way in which to faithfully relate visibilities during variable episodes, providing a time-averaged image of the Sgr A*. In the absence of an a priori accurate model for Sgr A*'s flares, this makes it possible to identify the qualitative features of the relevant processes.

Due to its much larger mass, what can be probed via astrometry for M87 is very different than what is accessible for Sgr A*. In M87's case, perturbations induced by the stellar/remnant cusp are negligible, as are displacements due to potential binary companions. Instead, the utility of astrometry with the EHT is the ability to relate the mm-VLBI image, in which the black hole is clearly identifiable due to its silhouette against nearby emission, and the large-scale structures in longer-wavelength images. This provides a way in which to conclusively locate the black hole, eliminating ambiguity in the identification of a putative counter jet, inclination, opening angle, nature of the radio core, and relationship between the black hole and the radio jet. Moreover, during dynamical periods, with the EHT it is possible to follow the creation and propagation of radio knots from sub-horizon to parsec scales, shedding light upon the source of the observed variability in M87 specifically, and AGN more generally.

We thank Irwin Shapiro, Sheperd Doeleman and Vincent Fish for enlightening discussions and suggestions. This research has made use of the NASA/IPAC Extragalactic Database (NED) which is operated by the Jet Propulsion Laboratory, California Institute of Technology, under contract with the National Aeronautics and Space Administration. This work was supported in part by NSF grant AST-0907890 and NASA grants NNX08AL43G and NNA09DB30A.

APPENDIX

A. MILLIMETER ISOPLANATIC ANGLE

Understanding atmospheric propagation effects is critical to high-fidelity image reconstruction at high frequencies. As a result, considerable effort has been expended theoretically and empirically characterizing the phase fluctuations associated with spatially varying indices of refraction in the turbulent atmosphere. A general treatment can be found in Thompson et al. (2001); here we collect some results that are of interest to mm-VLBI astrometry.

We wish to estimate the limits imposed by atmospheric propagation effects upon the accuracy with which the relative locations of nearby sources may be determined at 230 GHz (1.3 mm) and 345 GHz (0.87 mm). To do this we will make a number of simplifying approximations and convenient assumptions regarding the structure of the intervening atmosphere and the sources of interest. We begin by defining a model for the atmospheric fluctuations, and the associated phase errors along nearby lines of sight. After doing so, we will specify an idealized astrometric experiment, and compute the associated errors induced by the forgoing atmospheric model.

The atmospheric model is defined by fluctuations on top of some mean structure. We make the common assumption of a plane parallel atmosphere, imparting an average phase delay. Superimposed upon this are gaussian phase fluctuations, assumed to be due to a thin layer within the troposphere (fixed at an altitude of roughly $L \simeq 1\,\mathrm{km}$). The resulting phase perturbations are then characterized by the mean value and the spatial correlation function, commonly referred to as the structure function. These are defined by their zenith values:

$$\Phi_{Z} \equiv \langle \phi_{Z}(\mathbf{x}, t) \rangle,
\mathcal{D}_{\phi}(|\mathbf{d}|) \equiv \langle [\phi_{Z}(\mathbf{x} + \mathbf{d}, t) - \phi_{Z}(\mathbf{x}, t)]^{2} \rangle,
\Sigma_{\phi}^{2} \equiv \langle \phi_{Z}^{2}(\mathbf{x}, t) \rangle - \Phi_{Z}^{2} = \frac{1}{2} \mathcal{D}_{\phi}(\infty),$$
(A1)

where we have given the auto-correlation function a unique symbol despite being degenerate with the $\mathcal{D}_{\phi}(d)$, and \mathbf{d} will correspond to interferometer baselines. Each of these quantities is a property of the particular site and may be empirically determined. For example, Φ_Z may be obtained from various atmospheric models (e.g., Niell 1996; Boehm et al. 2006a,b), with typical values of $(600\,\mathrm{cm}/\lambda)\mathrm{rad}$ (though this varies by roughly a factor of two between sea level and 5000 m, the altitude of the ALMA and Hawaii sites). At small spatial separations the structure function has been found to be well fit by a power law, $\mathcal{D}_{\phi}(d)\simeq \left(2\pi\sigma_{d0}/\lambda\right)^2(d/1\,\mathrm{km})^{2\beta}\mathrm{rad}$ with values for σ_{d0} and β given in Table 2 for the relevant locations. At large d, $\mathcal{D}_{\phi}(d)$ asymptotes to a fixed value, $2\Sigma_{\phi}^2$. Typical values for Σ_{ϕ} are $0.01\Phi_Z\simeq(6\,\mathrm{cm}/\lambda)\mathrm{rad}$, is dominated by large-scale variations in the wet component and varies substantially on hourly timescales.

The phase perturbation along a general oblique line of sight, defined by a position on the sky α , associated with zenith angle $z_{\mathbf{X},\alpha}$ at location \mathbf{x} , in a plane-parallel geometry is given by

$$\phi_a(\mathbf{x}, \boldsymbol{\alpha}, t) = \phi_Z(\mathbf{x} + L \tan z_{\mathbf{X}, \boldsymbol{\alpha}}, t) \sec z_{\mathbf{X}, \boldsymbol{\alpha}}. \tag{A2}$$

From this we can construct an angular structure function:

$$\mathcal{D}_{\phi}(\boldsymbol{\alpha}, \boldsymbol{\delta}) \equiv \langle [\phi_{a}(\mathbf{x}, \boldsymbol{\alpha} + \boldsymbol{\delta}, t) - \phi_{a}(\mathbf{x}, \boldsymbol{\alpha}, t)]^{2} \rangle - \Phi_{Z}^{2} \sec^{2} z \tan^{2} z \, \delta z^{2}$$

$$\simeq \mathcal{D}_{\phi}(d) \sec^{2} z \left[1 + \tan z \, \delta z + \frac{1 + \sin^{2} z}{2 \cos z} \, \delta z^{2} \right] + \Sigma_{\phi}^{2} \sec^{2} z \tan^{2} z \, \delta z^{2} + \mathcal{O}\left(\delta z^{3}\right),$$
(A3)

where we have suppressed the subscripts on z and δz , which should be understood to be uniquely defined in terms of \mathbf{x} , α , and δ ,

$$d \equiv L\sqrt{\left[\tan(z+\delta z) - \tan z\right]^2 + \left|\delta\right|^2 - \delta z^2}$$

$$\simeq L\sqrt{\left(\sec^4 z - 1\right)\delta z^2 + \left|\delta\right|^2},$$
(A4)

Site Telescopes Alt. σ_{d0}^{a} Reference (mm) JCMT, SMA, CSO 4070 0.4 - 2.7 $0.4^{\circ} - 4.5^{\circ}$ Masson (1994) Mauna Keac 0.75 $0.6^{\circ} - 7.7^{\circ}$ $1.0^{\circ} - 6.6^{\circ}$ Chilec ASTE APEX ALMA 5000 0.3 - 1.5 $1.6^{\circ} - 11^{\circ}$ NRAO (1998) 5.3°-9.6° Plateau de Bure^c IRAM Interferometer 1.1-1.9 $4.3^{\circ} - 6.7^{\circ}$ Olmi & Downes (1992) 2552 0.3 - 0.7Cedar Flatd 0.5°-3.3° $0.3^{\circ} - 2.0^{\circ}$ CARMA 2196 0.8 - 3.8Woody et al. (2004)

Table 2 Phase Error Structure Function Parameters and Isoplanatic Angles at Potential EHT Stations

Note. — Adapted from Thompson et al. (2001), Table 13.3.

- a Defined at a baseline of 1 km.
- b Where no value was given, $\beta = 5/6$, consistent with Kolmogorov turbulence, was assumed. c Ranges indicate good/bad observing conditions (e.g., nighttime/daytime).

and we have made use of the Taylor expansion of $\sec(z+\delta z)$ to

$$\sec(z+\delta z) = \sec z \left[1 + \tan z \, \delta z + \frac{1 + \sin^2 z}{2 \cos z} \, \delta z^2 + \mathcal{O}\left(\delta z^3\right) \right]. \tag{A5}$$

Unlike $\mathcal{D}_{\phi}(d)$, which is completely defined by the small-scale structure of the troposphere, $\mathcal{D}_{\phi}(\alpha, \delta)$ has a contribution due to large-scale atmospheric variations as a result of the different path lengths along the two lines of sight, resulting from the slightly different zenith angles. Which term dominates in Equation (A3) depends upon the zenith angle, how strongly nearby atmospheric patches are correlated and the magnitude of the large-scale atmospheric fluctuations about the average phase delay.

To estimate the limits upon the accuracy this implies we consider a simplified astrometric experiment. Specifically, we will assume that the two sources of interest are monochromatic point sources separated by more than a beam width, though extension to more complicated source structures is straightforward. Furthermore, we focus only upon atmospheric phase errors, and explicitly neglect all other contributions. Finally, we will assume the experiment consists of two sets of antenna pairs, one pair located at x = 0 and the other pair at some position $\mathbf{x} = \mathbf{u}$, sufficiently far away such that the atmospheric errors are completely uncorrelated. With these assumptions, the voltages induced by the radio waves emitted by the two point sources, located at positions α and $\alpha + \delta$, at a pair of neighboring antennas at some position x, each viewing one of the sources, are

$$V_{A}(\mathbf{x},t) = E_{I} \exp \left\{ -i \left[\omega t + \frac{2\pi \mathbf{x}}{\lambda} \cdot \boldsymbol{\alpha} + \phi_{a}(\mathbf{x}, \boldsymbol{\alpha}, t) \right] \right\}$$

$$V_{B}(x,t) = E_{II} \exp \left\{ -i \left[\omega t + \frac{2\pi \mathbf{x}}{\lambda} \cdot (\boldsymbol{\alpha} + \boldsymbol{\delta}) + \phi_{a}(\mathbf{x}, \boldsymbol{\alpha} + \boldsymbol{\delta}, t) \right] \right\},$$
(A6)

where $E_{I,II}$ are two complex constants, $\phi_a(\mathbf{x}, \boldsymbol{\alpha}, t)$ are the random phase perturbations imparted by propagation through the atmosphere defined above, and the remaining term is the geometric phase delay that we seek to measure. Cross-correlating the antenna voltages along the long baselines produces correlation peaks for each source at time delays of

$$\tau_{A} = \frac{2\pi \mathbf{u}}{\lambda} \cdot \boldsymbol{\alpha} + \phi_{a,\mathbf{u}}(\boldsymbol{\alpha},t)$$

$$\tau_{B} = \frac{2\pi \mathbf{u}}{\lambda} \cdot (\boldsymbol{\alpha} + \boldsymbol{\delta}) + \phi_{a,\mathbf{u}}(\boldsymbol{\alpha} + \boldsymbol{\delta},t),$$
(A7)

where $\phi_{a,\mathbf{u}}(\boldsymbol{\alpha},t) \equiv \phi_a(\mathbf{u},\boldsymbol{\alpha},t) - \phi_a(\mathbf{0},\boldsymbol{\alpha},t)$, in which we have as-

sumed that the atmospheric phase delay varies slowly in comparison to the timescales over which the visibilities are measured. From these the relative positions of the point sources may be extracted in the normal way, obtaining an estimate of the projection of the angular distance between two sources along **u** of

$$\hat{\mathbf{u}} \cdot \boldsymbol{\delta}_{\text{obs}} \equiv \frac{\lambda}{2\pi u} (\tau_B - \tau_A) - \Delta$$

$$= \hat{\mathbf{u}} \cdot \boldsymbol{\delta} + \frac{\lambda}{2\pi u} \left[\phi_{a,\mathbf{u}}(\boldsymbol{\alpha} + \boldsymbol{\delta}, t) - \phi_{a,\mathbf{u}}(\boldsymbol{\alpha}, t) \right] - \Delta$$

$$= \hat{\mathbf{u}} \cdot \boldsymbol{\delta} + \frac{\lambda}{2\pi u} \left\{ \left[\phi_a(\mathbf{u}, \boldsymbol{\alpha} + \boldsymbol{\delta}, t) - \phi_a(\mathbf{u}, \boldsymbol{\alpha}, t) \right] - \left[\phi_a(\mathbf{0}, \boldsymbol{\alpha} + \boldsymbol{\delta}, t) - \phi_a(\mathbf{0}, \boldsymbol{\alpha}, t) \right] \right\} - \Delta,$$
(A8)

where $\Delta \equiv \Phi_Z \sec z \tan z \delta z|_{\mathbf{u}} - \Phi_Z \sec z \tan z \delta z|_{\mathbf{0}}$ is the angular shift due to the differential phase delays at the two stations associated with the mean atmospheric model. The $\hat{\mathbf{u}} \cdot \boldsymbol{\delta}_{\rm obs}$ is a gaussian random variable centered upon the true value and with a variance due to the atmospheric phase fluctuations of

$$\sigma_{\delta}^{2} = \left(\frac{\lambda}{2\pi u}\right)^{2} \left[\left. \mathcal{D}_{\phi}(\alpha, \delta) \right|_{\mathbf{0}} + \left. \mathcal{D}_{\phi}(\alpha, \delta) \right|_{\mathbf{u}} \right]. \tag{A9}$$

This has contributions from both, the small-scale, rapidly varying structures that limit the atmospheric coherence time (the $\mathcal{D}_{\phi}(d)$ terms in Equation (A3)), and large-scale, slowly evolving fluctuations (responsible for the Σ_{ϕ} terms in Equation (A3)). Because β is typically close to unity, which dominates the astrometric uncertainty is only weakly dependent upon the angular separation of the two sources. In the remainder of this section we discuss the two kinds of terms separately.

The error term associated with the rapidly varying, smallscale structures due to a single station is given by

$$\sigma_s \lesssim \frac{\lambda}{u} \frac{\sigma_{d0}}{\lambda} \sec z \left(\frac{L}{1 \, \text{km}} \sec^2 z \, \delta z\right)^{\beta}$$
, (A10)

where we have chosen $\delta z = |\delta|$, resulting in the maximum σ_s for a given angular separation. For a values of σ_{d0} , β , and z typical of the stations likely to be employed by the EHT, at 1.3 mm, $\sigma_s \lesssim 0.5 (\lambda/u) (L/1 \,\mathrm{km})^{\beta} (\delta z/1^{\circ})^{\beta}$.

Since σ_s is dominated by contributions from the most rapidly varying structures in the atmosphere, observations separated in time by more than the atmospheric coherence time probe independent realizations of the atmospheric turbulence. As a consequence, during a few hour observing period it is possible to reduce σ_s by an order of magnitude. Thus, the limit upon δ imposed by a given astrometric tolerance, σ_A , and N independent

d Ranges indicate before and after water vapor radiometry has been employed.

observations is

$$\delta \lesssim \delta_0 \equiv 57^{\circ} \cos^2 z \left(\frac{L}{1 \,\mathrm{km}}\right)^{-1} \left(\sqrt{N} \cos z \frac{u \sigma_A}{\sigma_{d0}}\right)^{1/\beta} \tag{A11}$$

Limits for N=1 and $\sigma_A=\lambda/u$ are listed in Table 2 for 1.3 mm and 0.87 mm for $z=70^\circ$, typical of the zenith angle for Sgr A* as seen from North American sites (the most pessimistic scenario we consider). In terms of these, we have

$$\sigma_s \simeq \frac{2.9\cos z}{\sqrt{N}} \left(0.12\sec^2 z \frac{\delta}{\delta_0}\right)^{\beta} \frac{\lambda}{u}.$$
 (A12)

The error associated with the large-scale, slowly evolving component at a single station is given by

$$\sigma_l \simeq \frac{\lambda}{u} \frac{\Sigma_\phi}{2\pi} \sec z \tan z \, \delta z.$$
 (A13)

For Sgr A* viewed from North America, typically $\sigma_l \lesssim (\lambda/u)(\delta z/1^\circ)$, can be substantially smaller at high-altitude sites, and is a strong function of zenith angle.

Unlike the small-scale component, the long timescale over which the large-scale structures vary means that only a handful of independent realizations will be encountered on a given night. Thus, substantially reducing σ_l by integrating over long times requires observations spanning many days at least. However, as we discuss in the main text, the large spatial and temporal scales of these fluctuations make possible a number of schemes to measure the additional path delay directly and significantly reduce the unmodeled Σ_{ϕ} . For this reason the uncertainty in the angular separation due to unmodeled slowly varying and rapidly varying components,

$$\sigma_{\delta}^2 = \sigma_s^2 |_{\mathbf{0}} + \sigma_l^2 |_{\mathbf{0}} + \sigma_s^2 |_{\mathbf{u}} + \sigma_l^2 |_{\mathbf{u}}, \qquad (A14)$$

are likely to be similar.

B. MULTI-REFERENCE ASTROMETRIC CALIBRATION

Here we describe explicitly a scheme to measure and remove the contribution to the astrometric uncertainty arising from slowly varying, large-scale atmospheric fluctuations (i.e., those responsible for the σ_l terms in the preceding appendix). The method utilizes multiple nearby reference sources to measure the slowly-varying phase fluctuations, which may then be explicitly accounted for in the astrometric measurement of interest. The viability of the scheme is predicated upon the following assumptions:

- The existence of a set of at least three reference sources near the target source with different zenith angles at each VLBI station. Note that the limitations upon the separation derived in Section A may be substantially relaxed since both σ_l and σ_s are both roughly proportional to $|\delta|$, and thus the limit upon the fractional accuracy imposed by rapidly-varying, short timescale atmospheric fluctuations is only weakly dependent upon separation. In practice $|\delta|$ is limited by the size of the region over which the large-scale phase perturbations are uniform, which is typically many degrees.
- Over the portion of the sky of interest, the large-scale atmospheric phase delays at each site is well modeled by a single-parameter model (e.g., the sec z model we will employ here).

- The reference sources do not evolve intrinsically or relative to each other. More specifically, the angular separation between each of the reference sources is fixed.
- The "true" angular separations of the reference sources can be measured with the desired fractional accuracy.
 This may be accomplished, e.g., by careful atmospheric modeling and long-time integrations.

To illustrate the procedure, and estimate the resulting calibration uncertainties we consider observations of three reference sources on a single, static baseline. We use the letters A, B, and C to indicate a particular source, and numbers 1 and 2 to indicate the locations of individual mm-VLBI stations. For shorthand we define $\Delta \sec z|_{B1}^{A1} = \sec z_{A1} - \sec z_{B1}$ to be the difference between the secant of the zenith angle of reference sources A and B as seen from station 1, with similar expressions for all sources and both stations. In terms of these, following the previous appendix, from a single observation we have an estimate of the separation of reference sources A and B of:

$$\hat{\mathbf{u}}_{12} \cdot \boldsymbol{\delta}_{AB,\text{obs}} = \hat{\mathbf{u}}_{12} \cdot \boldsymbol{\delta}_{AB} + \Delta \delta_{s,AB}
+ \frac{\lambda}{2\pi u_{12}} \Delta \Phi_1 \Delta \sec z|_{B1}^{A1} - \frac{\lambda}{2\pi u_{12}} \Delta \Phi_2 \Delta \sec z|_{B2}^{A2}, \quad (B1)$$

where we have separated the contributions to the phase fluctuation into modeled large-scale and the remaining unmodeled small-scale fluctuations ($\Delta \delta_s$). The $\Delta \Phi_{1,2}$ are the unknown zenith phase delays implied at stations 1 and 2, respectively, associated with the large-scale atmospheric perturbations. Since δ_{AB} is known, or may be measured by comparing data sets taken over many days, we may invert this to obtain an expression for the unknown $\Delta \Phi_{1,2}$:

$$\Delta\Phi_{1} \Delta \sec z|_{B1}^{A1} - \Delta\Phi_{2} \Delta \sec z|_{B2}^{A2}$$

$$= \frac{2\pi}{\lambda} \left[\mathbf{u}_{12} \cdot \left(\boldsymbol{\delta}_{AB,\text{obs}} - \boldsymbol{\delta}_{AB} \right) - \Delta \boldsymbol{\delta}_{s,AB} \right]$$

$$\Delta\Phi_{1} \Delta \sec z|_{C1}^{B1} - \Delta\Phi_{2} \Delta \sec z|_{C2}^{B2}$$

$$= \frac{2\pi}{\lambda} \left[\mathbf{u}_{12} \cdot \left(\boldsymbol{\delta}_{BC,\text{obs}} - \boldsymbol{\delta}_{BC} \right) - \Delta \boldsymbol{\delta}_{s,BC} \right]$$

$$\Delta\Phi_{1} \Delta \sec z|_{A1}^{C1} - \Delta\Phi_{2} \Delta \sec z|_{A2}^{C2}$$

$$= \frac{2\pi}{\lambda} \left[\mathbf{u}_{12} \cdot \left(\boldsymbol{\delta}_{CA,\text{obs}} - \boldsymbol{\delta}_{CA} \right) - \Delta \boldsymbol{\delta}_{s,CA} \right],$$
(B2)

where we have added analogous terms for the other source pairs. In principle, these are degenerate, providing only two linearly independent equations for $\Delta\Phi_1$ and $\Delta\Phi_2$. In practice, since the $\Delta\delta_s$ terms are dominated by the small-scale atmospheric structure, this degeneracy is weakly broken, providing an external estimate of the magnitude of the $\Delta\delta_s$ terms. Considering only the first two, we obtain an estimate for $\Delta\Phi_1$ of

$$\frac{\Delta\Phi_{1} =}{\frac{2\pi\mathbf{u}_{12}}{\lambda} \cdot \frac{\Delta\sec z|_{B2}^{A2}\left(\boldsymbol{\delta}_{AB,\text{obs}} - \boldsymbol{\delta}_{AB}\right) - \Delta\sec z|_{C2}^{B2}\left(\boldsymbol{\delta}_{BC,\text{obs}} - \boldsymbol{\delta}_{BC}\right)}{\Delta\sec z|_{B2}^{A2}\Delta\sec z|_{C1}^{B1} - \Delta\sec z|_{B1}^{A1}\Delta\sec z|_{C2}^{B2}} }$$
(B3)

with a similar expression for $\Delta\Phi_2$ obtained by transposing 1 and 2 everywhere. Comparing this to Equation (B2), assuming that the errors in the $\delta_{AB,BC}$ may be neglected in comparison to $\Delta\delta_s$ (the errors in the zenith angle estimates result in higher-order corrections, and thus always may be ignored), we find a

variance in $\Delta\Phi_1$ induced by the small-scale, rapid variability of

$$\sigma_{\Delta\Phi_{1}}^{2} \simeq \frac{\left(\Delta \sec z|_{B2}^{A2}\right)^{2} \sigma_{s,AB}^{2} + \left(\Delta \sec z|_{C2}^{B2}\right)^{2} \sigma_{s,BC}^{2}}{\left(\Delta \sec z|_{B2}^{A2} \Delta \sec z|_{C1}^{B1} - \Delta \sec z|_{B1}^{A1} \Delta \sec z|_{C2}^{B2}\right)^{2}},$$
(B4)

with a similar expression for $\sigma^2_{\Delta\Phi_2}$. Note that if all of the reference sources lie at similar zenith angles, and have similar separations in zenith angle from each other, this reduces to $\sigma_{\Delta\Phi_{1,2}} \sim \sigma_s$, and thus the fractional precision of the large-scale phase corrections is comparable to that associated with the small-scale, rapidly varying fluctuations over hour-long integrations, roughly 1 μ as. The accuracy will be limited by how well the true separations of the reference sources can be measured, presumably by averaging over long times, and the validity of the assumptions underlying the scheme.

C. POSITION JITTER POWER SPECTRUM

Supermassive black holes settle via dynamical friction into the center of their galactic potential well on timescales short in comparison to the Hubble time (Chatterjee et al. 2002). Nevertheless, fluctuations in the surrounding stellar/remnant⁸ distribution induce random displacements of the central black hole similar to Brownian motion. Here we derive an estimate of the displacement power spectrum. For simplicity we assume that the surrounding distribution of gravitating bodies is spherically symmetric, with number density n(r) and mass function $\phi(m,r)$, all orbits are circular, and that dynamical collective N-body effects are unimportant, i.e., the fluctuations about the mean density may be approximated by Poisson statistics. This last assumption may not be strictly justified in the spherical case, though is in the more generic triaxial situation.

In the vicinity of the supermassive black hole, we may approximate the black hole's motion by

$$\ddot{\mathbf{x}} + \gamma \dot{\mathbf{x}} + \omega_0^2 \mathbf{x} = \mathbf{a}(t), \tag{C1}$$

where ${\bf x}$ is the location of the black hole, ${\bf a}$ is the fluctuating acceleration induced by perturbations in the surrounding stellar distribution, $\omega_0^2 \equiv d^2\Phi/dr^2$ is the natural frequency of oscillation in the bottom of the galactic potential well, and γ is the damping associated with dynamical friction. We may estimate ω_0 in terms of the stellar density at the galactic center:

$$\omega_0^2 \simeq \frac{4\pi}{3} G \rho_0 \tag{C2}$$

where ρ_0 is the average stellar density within the region of influence. Thus, ω_0 is a proxy for the stellar mass density within the core. The dynamical damping rate is approximately given by

$$\gamma \simeq 4\sqrt{2\pi} \ln \Lambda G^2 M \frac{\rho_0}{\sigma_0^3} \tag{C3}$$

where $\ln \Lambda$ is the Coulomb integral, M is the mass of the central supermassive black hole, and σ_0 is the stellar velocity dispersion in the stellar core (Chatterjee et al. 2002). Typically, we will be interested in the case when $\omega \gg \omega_0$, γ , though we have kept all terms in the interest of generality.

Since the system is spherically symmetric, we will focus only upon the displacement along the $\hat{\mathbf{x}}$ direction. In this case, the power spectrum of these displacements is then given by

$$P_{x,\omega} = \langle |x_{\omega}|^2 \rangle = \frac{P_{a,\omega}}{(\omega^2 - \omega_0^2)^2 + \gamma^2 \omega^2} \simeq \omega^{-4} P_{a,\omega} , \qquad (C4)$$

where $P_{a,\omega}$ is the power spectrum of the fluctuating accelerations. Thus, computing the spectrum of displacements is reduced to computing the spectrum of the fluctuating forces.

In Chatterjee et al. (2002) it was assumed that the fluctuations were completely uncorrelated in time, i.e., that $P_{a,\omega}$ was constant. For virialized systems this may be derived directly via the fluctuation dissipation theorem. However, this is likely to be a poor approximation in the case of interest, where we are interested exclusively in short-timescale variations in the position of the supermassive black hole. Thus we approach the problem phenomenologically: given a density profile we estimate the $P_{a,\omega}$ associated with Poisson fluctuations in the number density of stars.

We begin by considering a thin shell of width Δr centered upon a radius r. Within this shell there are $N=4\pi r^2 n(r)\Delta r$ objects, with mass function $\phi(m,r)$, randomly distributed. The induced acceleration along the $\hat{\mathbf{x}}$ -axis is then

$$a = -\sum_{i=1}^{N} \frac{Gm_i x_i}{r^3}, \tag{C5}$$

from which it is obvious that $\langle a \rangle = 0$. The variance in the acceleration is

$$\langle a^{2} \rangle = \langle \sum_{i,j=1}^{N} \frac{G^{2} m_{i} m_{j} x_{i} x_{j}}{r^{3}} \rangle = \frac{G^{2}}{r^{6}} \sum_{i,j=1}^{N} \langle m_{i} m_{j} \rangle \langle x_{i} x_{j} \rangle$$

$$= \frac{G^{2}}{3r^{4}} \sum_{i=1}^{N} \langle m_{i}^{2} \rangle = \frac{G^{2} \mu^{2}}{3r^{4}} N,$$
(C6)

where $\langle x_i x_j \rangle = r^2 \delta_{ij}/3$ was used and $\mu^2(r) \equiv \int_0^\infty dm m^2 \phi(m,r)$. Over densities within the shell will persist until the orbits of stars within the shell can re-randomize the stars. Therefore, unlike Chatterjee et al. (2002), we expect these perturbations to be correlated for a time comparable to $1/\Omega_k(r)$, where $\Omega_k(r)$ is the Keplerian angular velocity at r. Thus, the auto-correlation function of the acceleration fluctuations is approximately

$$R_{a,T}^{\Delta r} \equiv \langle a(t)a(t+T)\rangle \simeq \langle a^2\rangle e^{-\Omega_k^2 T^2/2} = \frac{G^2 \mu^2}{3r^4} N e^{-\Omega_k^2 T^2/2}.$$
 (C7)

This implies a power spectrum associated with the shell of stars of

$$P_{a,\omega}^{\Delta r} \simeq \frac{2(2\pi)^{3/2}}{3} \frac{G^2 \mu^2}{r^2} \frac{n}{\Omega_k} e^{-\omega^2/2\Omega_k^2} \Delta r.$$
 (C8)

Since we have already assumed that the positions of individual stars are uncorrelated (when we assumed Poisson statistics within a shell), the power spectrum of the entire distribution of stars may then be constructed by summing multiple shells, i.e.,

$$P_{a,\omega} = \int_0^\infty dr \, \frac{2(2\pi)^{3/2}}{3} \frac{G^2 \mu^2}{r^2} \frac{n}{\Omega_k} e^{-\omega^2/2\Omega_k^2} \,, \tag{C9}$$

which may be inserted into Equation (C4) to obtain the desired power spectrum.

⁸ Henceforth, for simplicity we will refer to the "stellar" distribution, "stellar" mass, and "stars" though this should be understood to include evolved objects like stellar mass black holes as well.

To make further progress we must choose $\phi(m,r)$ and n(r). From these we may then construct the Ω_k :

$$\Omega_k^2(r) = \frac{GM}{r^3} + \frac{G}{r^3} \int_0^\infty dr \int_0^\infty dm \, m\phi(m, r) n(r) \,, \qquad (C10)$$

and thus $P_{x,\omega}$.

REFERENCES

Acciari, V. A., et al. 2009, Science, 325, 444

Alexander, T., & Hopman, C. 2009, ApJ, 697, 1861

Amaro-Seoane, P., & Preto, M. 2010, ArXiv e-prints

Anderson, J. M., Ulvestad, J. S., & Ho, L. C. 2004, ApJ, 603, 42

Backer, D. C., & Sramek, R. A. 1999, ApJ, 524, 805

Bartko, H., et al. 2009, New Ast. Rev., 53, 301

Becker, R. H., White, R. L., & Edwards, A. L. 1991, ApJS, 75, 1

Begelman, M. C., Blandford, R. D., & Rees, M. J. 1980, Nature, 287, 307

Bennett, C. L., Lawrence, C. R., Burke, B. F., Hewitt, J. N., & Mahoney, J. 1986, ApJS, 61, 1

Biretta, J. A., Sparks, W. B., & Macchetto, F. 1999, ApJ, 520, 621

Boehm, J., Niell, A., Tregoning, P., & Schuh, H. 2006a, Geophys. Res. Lett., 33, 7304

Boehm, J., Werl, B., & Schuh, H. 2006b, Journal of Geophysical Research (Solid Earth), 111, 2406

Bogdanović, T., Eracleous, M., & Sigurdsson, S. 2009, ApJ, 697, 288

Boroson, T. A., & Lauer, T. R. 2009, Nature, 458, 53

Bower, G. C., Backer, D. C., & Sramek, R. A. 2001, ApJ, 558, 127 Bower, G. C., Backer, D. C., Zhao, J., Goss, M., & Falcke, H. 1999, ApJ, 521,

Bower, G. C., Falcke, H., Sault, R. J., & Backer, D. C. 2002, ApJ, 571, 843 Braun, R., Oosterloo, T. A., Morganti, R., Klein, U., & Beck, R. 2007, A&A, 461, 455

Broderick, A. E., Fish, V. L., Doeleman, S. S., & Loeb, A. 2009a, ApJ, 697, 45 -. 2010, ApJ

Broderick, A. E., & Loeb, A. 2005, MNRAS, 363, 353

-. 2006, MNRAS, 367, 905

-. 2009, ApJ, 697, 1164

Broderick, A. E., Loeb, A., & Narayan, R. 2009b, ApJ, 701, 1357

Buchholz, R. M., Schödel, R., & Eckart, A. 2009, A&A, 499, 483

Byun, S. H., & Bar-Sever, Y. E. 2009, Journal of Geodesy, 83, 367

Cara, M., & Lister, M. L. 2008, ApJ, 674, 111

Caswell, J. L., Breen, S. L., & Ellingsen, S. P. 2010, MNRAS, 1488

Chatterjee, P., Hernquist, L., & Loeb, A. 2002, ApJ, 572, 371

Cohen, A. S., Lane, W. M., Cotton, W. D., Kassim, N. E., Lazio, T. J. W., Perley, R. A., Condon, J. J., & Erickson, W. C. 2007, AJ, 134, 1245

Condon, J. J., Cotton, W. D., & Broderick, J. J. 2002, AJ, 124, 675

Condon, J. J., Cotton, W. D., Greisen, E. W., Yin, Q. F., Perley, R. A., Taylor, G. B., & Broderick, J. J. 1998, AJ, 115, 1693

Condon, J. J., & Jauncey, D. L. 1974, AJ, 79, 1220

Counselman, III, C. C., Kent, S. M., Knight, C. A., Shapiro, I. I., Clark, T. A., Hinteregger, H. F., Rogers, A. E. E., & Whitney, A. R. 1974, Physical Review Letters, 33, 1621

Covey, K. R., et al. 2008, AJ, 136, 1778

Dale, D. A., et al. 2005, ApJ, 633, 857

Decarli, R., Dotti, M., Montuori, C., Liimets, T., & Ederoclite, A. 2010, ApJ,

Dexter, J., Agol, E., Fragile, P. C., & McKinney, J. C. 2010, ApJ, 717, 1092 Do, T., Ghez, A. M., Morris, M. R., Lu, J. R., Matthews, K., Yelda, S., & Larkin, J. 2009, ApJ, 703, 1323

Do, T., Ghez, A. M., Morris, M. R., Lu, J. R., Matthews, K., Yelda, S., Wright, S., & Larkin, J. 2010, ArXiv e-prints

Doeleman, S., et al. 2009a, in Astronomy, Vol. 2010, astro2010: The Astronomy and Astrophysics Decadal Survey, 68-+

Doeleman, S. S., Fish, V. L., Broderick, A. E., Loeb, A., & Rogers, A. E. E. 2009b, ApJ, 695, 59

Doeleman, S. S., et al. 2008, Nature, 455, 78

Doi, A., Kameno, S., Kohno, K., Nakanishi, K., & Inoue, M. 2005, MNRAS, 363, 692

Douglas, J. N., Bash, F. N., Bozyan, F. A., Torrence, G. W., & Wolfe, C. 1996, AJ, 111, 1945

Dressel, L. L., & Condon, J. J. 1978, ApJS, 36, 53

Eckart, A., et al. 2006, A&A, 450, 535

Ekers, J. A. 1969, Australian Journal of Physics Astrophysical Supplement, 7,

Escala, A., Larson, R. B., Coppi, P. S., & Mardones, D. 2004, ApJ, 607, 765

-. 2005, ApJ, 630, 152

Filho, M. E., Fraternali, F., Markoff, S., Nagar, N. M., Barthel, P. D., Ho, L. C., & Yuan, F. 2004, A&A, 418, 429

Fish, V. L., Doeleman, S. S., Broderick, A. E., Loeb, A., & Rogers, A. E. E. 2009, ApJ, 706, 1353

Fish, V. L., et al. 2011, ApJ, 727, L36

Flesch, E. 2010, Pub. Astr. Soc. Aus., 27, 283

Fomalont, E. B. 2005, in Astronomical Society of the Pacific Conference Series, Vol. 340, Future Directions in High Resolution Astronomy, ed. J. Romney & M. Reid, 460-+

Freitag, M., Amaro-Seoane, P., & Kalogera, V. 2006, ApJ, 649, 91

Fujii, M., Iwasawa, M., Funato, Y., & Makino, J. 2009, ApJ, 695, 1421 -. 2010, ApJ, 716, L80

Gair, J. R., Barack, L., Creighton, T., Cutler, C., Larson, S. L., Phinney, E. S., & Vallisneri, M. 2004, Classical and Quantum Gravity, 21, 1595

Gair, J. R., Tang, C., & Volonteri, M. 2010, Phys. Rev. D, 81, 104014

Gallimore, J. F., Axon, D. J., O'Dea, C. P., Baum, S. A., & Pedlar, A. 2006, AJ, 132, 546

Gebhardt, K., Adams, J., Richstone, D., Lauer, T. R., Faber, S. M., Gultekin, K., Murphy, J., & Tremaine, S. 2011, ArXiv:1101.1954

Gebhardt, K., & Thomas, J. 2009, ApJ, 700, 1690

Geldzahler, B. J., & Witzel, A. 1981, AJ, 86, 1306

Gendre, M. A., & Wall, J. V. 2008, MNRAS, 390, 819

Genzel, R., Pauliny-Toth, I. I. K., Preuss, E., & Witzel, A. 1976, AJ, 81, 1084

Genzel, R., et al. 2003, ApJ, 594, 812 Gerhard, O. 2001, ApJ, 546, L39

Ghez, A. M., et al. 2003, ApJ, 586, L127

2008, ApJ, 689, 1044

Giannios, D., Uzdensky, D. A., & Begelman, M. C. 2010, MNRAS, 402, 1649 Gillessen, S., Eisenhauer, F., Fritz, T. K., Bartko, H., Dodds-Eden, K., Pfuhl, O., Ott, T., & Genzel, R. 2009a, ApJ, 707, L114

Gillessen, S., Eisenhauer, F., Trippe, S., Alexander, T., Genzel, R., Martins, F., & Ott, T. 2009b, ApJ, 692, 1075

Gower, J. F. R., Scott, P. F., & Wills, D. 1967, MmRAS, 71, 49

Gregory, P. C., & Condon, J. J. 1991, ApJS, 75, 1011

Gregory, P. C., Scott, W. K., Douglas, K., & Condon, J. J. 1996, ApJS, 103,

Gualandris, A., & Merritt, D. 2009, ApJ, 705, 361

Hansen, B. M. S., & Milosavljević, M. 2003, ApJ, 593, L77

Healey, S. E., Romani, R. W., Taylor, G. B., Sadler, E. M., Ricci, R., Murphy, T., Ulvestad, J. S., & Winn, J. N. 2007, ApJS, 171, 61

Heeschen, D. S., & Conklin, E. K. 1975, ApJ, 196, 347

Heeschen, D. S., & Wade, C. M. 1964, AJ, 69, 277

Honma, M., Kawaguchi, N., & Sasao, T. 2000, in Society of Photo-Optical Instrumentation Engineers (SPIE) Conference Series, Vol. 4015, Society of Photo-Optical Instrumentation Engineers (SPIE) Conference Series, ed. H. R. Butcher, 624-631

Hopman, C., & Alexander, T. 2005, ApJ, 629, 362

2006, ApJ, 645, L133

Horiuchi, S., et al. 2004, ApJ, 616, 110

Huang, L., Takahashi, R., & Shen, Z. 2009, ApJ, 706, 960

Humphreys, E. M. L. 2007, in IAU Symposium, Vol. 242, IAU Symposium, ed. J. M. Chapman & W. A. Baan, 471-480

Imai, H., et al. 1997, A&A, 317, L67

Isaacman, R., Wouterloot, J. G. A., & Habing, H. J. 1980, A&A, 86, 254

Junor, W., Biretta, J. A., & Livio, M. 1999, Nature, 401, 891

Kawaguchi, N., Sasao, T., & Manabe, S. 2000, in Society of Photo-Optical Instrumentation Engineers (SPIE) Conference Series, Vol. 4015, Society of Photo-Optical Instrumentation Engineers (SPIE) Conference Series, ed. H. R. Butcher, 544-551

Kellermann, K. I., & Pauliny-Toth, I. I. K. 1973, AJ, 78, 828

Kellermann, K. I., Pauliny-Toth, I. I. K., & Williams, P. J. S. 1969, ApJ, 157, 1 Kellermann, K. I., et al. 2004, ApJ, 609, 539

Kim, S. S., Figer, D. F., & Morris, M. 2004, ApJ, 607, L123

Kovalev, Y. Y., Lister, M. L., Homan, D. C., & Kellermann, K. I. 2007, ApJ,

Kovalev, Y. Y., et al. 2005, AJ, 130, 2473

Krichbaum, T. P., Graham, D. A., Bremer, M., Alef, W., Witzel, A., Zensus, J. A., & Eckart, A. 2006, J. Phys. Conf. Series, 54, 328

Krichbaum, T. P., et al. 1997, A&A, 323, L17

Krips, M., et al. 2007, A&A, 464, 553

Kuehr, H., Witzel, A., Pauliny-Toth, I. I. K., & Nauber, U. 1981, A&AS, 45,

Large, M. I., Mills, B. Y., Little, A. G., Crawford, D. F., & Sutton, J. M. 1981, MNRAS, 194, 693

Laurent-Muehleisen, S. A., Kollgaard, R. I., Ryan, P. J., Feigelson, E. D., Brinkmann, W., & Siebert, J. 1997, A&AS, 122, 235

Ledlow, M. J., & Owen, F. N. 1995, AJ, 109, 853

Lee, S., Lobanov, A. P., Krichbaum, T. P., Witzel, A., Zensus, A., Bremer, M., Greve, A., & Grewing, M. 2008, AJ, 136, 159

Leeuw, L. L., Sansom, A. E., & Robson, E. I. 2000, MNRAS, 311, 683

Leeuw, L. L., Sansom, A. E., Robson, E. I., Haas, M., & Kuno, N. 2004, ApJ, 612, 837

Levin, Y., Wu, A., & Thommes, E. 2005, ApJ, 635, 341

Lister, M. L., & Homan, D. C. 2005, AJ, 130, 1389

Liu, X., Shen, Y., Strauss, M. A., & Greene, J. E. 2010, ApJ, 708, 427

Lonsdale, C. J., Doeleman, S. S., & Phillips, R. B. 1998, AJ, 116, 8

Ly, C., Walker, R. C., & Junor, W. 2007, ApJ, 660, 200

Ly, C., Walker, R. C., & Wrobel, J. M. 2004, AJ, 127, 119

Marrone, D. P., et al. 2008, ApJ, 682, 373

Marscher, A. P., et al. 2008, Nature, 452, 966

Masson, C. R. 1994, in Astronomical Society of the Pacific Conference Series, Vol. 59, IAU Colloq. 140: Astronomy with Millimeter and Submillimeter Wave Interferometry, ed. M. Ishiguro & J. Welch, 87—+

McMillan, S. L. W., & Portegies Zwart, S. F. 2003, ApJ, 596, 314

Menten, K. M., Reid, M. J., Eckart, A., & Genzel, R. 1997, ApJ, 475, L111+ Merritt, D. 2010, ApJ, 718, 739

Merritt, D., Gualandris, A., & Mikkola, S. 2009, ApJ, 693, L35

Merritt, D., & Poon, M. Y. 2004, ApJ, 606, 788

Meyer, L., Schödel, R., Eckart, A., Karas, V., Dovčiak, M., & Duschl, W. J. 2006, A&A, 458, L25

Miller, M. C., et al. 2009, in Astronomy, Vol. 2010, astro2010: The Astronomy and Astrophysics Decadal Survey, 210—+

Milosavljević, M., & Merritt, D. 2003, ApJ, 596, 860

Miralda-Escudé, J., & Gould, A. 2000, ApJ, 545, 847

Morris, M. 1993, ApJ, 408, 496

Mościbrodzka, M., Gammie, C. F., Dolence, J. C., Shiokawa, H., & Leung, P. K. 2009, ApJ, 706, 497

Nagar, N. M., Falcke, H., & Wilson, A. S. 2005, A&A, 435, 521

Nagar, N. M., Falcke, H., Wilson, A. S., & Ulvestad, J. S. 2002, A&A, 392, 53

Nagar, N. M., Wilson, A. S., & Falcke, H. 2001, ApJ, 559, L87

Niell, A. E. 1996, J. Geophys. Res., 101, 3227

Nord, M. E., Lazio, T. J. W., Kassim, N. E., Hyman, S. D., LaRosa, T. N., Brogan, C. L., & Duric, N. 2004, AJ, 128, 1646

NRAO. 1998, Recommended Site for the Millimeter Array, Tech. rep., National Radio Astronomy Observatory

Ochsenbein, F., Bauer, P., & Marcout, J. 2000, A&AS, 143, 23

O'Leary, R. M., Kocsis, B., & Loeb, A. 2009, MNRAS, 395, 2127

Olmi, L., & Downes, D. 1992, A&A, 262, 634

Pauliny-Toth, I. I. K., & Kellermann, K. I. 1972, AJ, 77, 797

Pauliny-Toth, I. I. K., Wade, C. M., & Heeschen, D. S. 1966, ApJS, 13, 65

Pauliny-Toth, I. I. K., Witzel, A., Preuss, E., Kühr, H., Kellermann, K. I., Fomalont, E. B., & Davis, M. M. 1978, AJ, 83, 451

Perets, H. B., & Alexander, T. 2008, ApJ, 677, 146

Pilkington, J. D. H., & Scott, P. F. 1965, MmRAS, 69, 183

Porquet, D., et al. 2008, A&A, 488, 549

Qin, S., Zhao, J., Moran, J. M., Marrone, D. P., Patel, N. A., Wang, J., Liu, S., & Kuan, Y. 2008, ApJ, 677, 353

Reich, W., Fürst, E., Reich, P., Kothes, R., Brinkmann, W., & Siebert, J. 2000, A&A, 363, 141

Reid, M. J., Biretta, J. A., Junor, W., Muxlow, T. W. B., & Spencer, R. E. 1989, ApJ, 336, 112

Reid, M. J., Broderick, A. E., Loeb, A., Honma, M., & Brunthaler, A. 2008, ApJ, 682, 1041

Reid, M. J., & Brunthaler, A. 2004, ApJ, 616, 872

Reid, M. J., & Brunthaler, A. 2005, in Astronomical Society of the Pacific Conference Series, Vol. 340, Future Directions in High Resolution Astronomy, ed. J. Romney & M. Reid, 253—+ Reid, M. J., & Menten, K. M. 2007, ApJ, 671, 2068

Reid, M. J., Menten, K. M., Genzel, R., Ott, T., Schödel, R., & Eckart, A. 2003, ApJ, 587, 208

Reid, M. J., Menten, K. M., Trippe, S., Ott, T., & Genzel, R. 2007, ApJ, 659, 378

Reid, M. J., Menten, K. M., Zheng, X. W., Brunthaler, A., & Xu, Y. 2009, ApJ, 705, 1548

Reid, M. J., & Moran, J. M. 1981, ARA&A, 19, 231

Reid, M. J., Readhead, A. C. S., Vermeulen, R. C., & Treuhaft, R. N. 1999a, ApJ, 524, 816

—. 1999b, ApJ, 524, 816

Roos, N. 1981, A&A, 104, 218

Roy, S., Rao, A. P., & Subrahmanyan, R. 2005, MNRAS, 360, 1305

Schödel, R., et al. 2007, A&A, 469, 125

Schönrich, R., Binney, J., & Dehnen, W. 2010, MNRAS, 403, 1829

Schutz, B. F., Centrella, J., Cutler, C., & Hughes, S. A. 2009, in Astronomy, Vol. 2010, astro2010: The Astronomy and Astrophysics Decadal Survey, 265—+

Shimmins, A. J., Bolton, J. G., & Wall, J. V. 1975, Australian Journal of Physics Astrophysical Supplement, 34, 63

Sigurdsson, S., & Rees, M. J. 1997, MNRAS, 284, 318

Slee, O. B. 1995, Australian Journal of Physics, 48, 143

Slee, O. B., & Higgins, C. S. 1973, Australian Journal of Physics Astrophysical Supplement, 27, 1

Sramek, R. 1975, AJ, 80, 771

Stull, M. A. 1971, AJ, 76, 1

Thompson, A. R., Moran, J. M., & Swenson, Jr., G. W. 2001, Interferometry and Synthesis in Radio Astronomy, 2nd Edition, ed. Thompson, A. R., Moran, J. M., & Swenson, G. W., Jr.

Ulvestad, J. S., & Ho, L. C. 2001, ApJ, 562, L133

Véron, P. 1977, A&AS, 30, 131

Veron-Cetty, M. P., & Veron, P. 1983, A&AS, 53, 219

Vollmer, B., Thierbach, M., & Wielebinski, R. 2004, A&A, 418, 1

Wagner, R. M., et al. 2009, ArXiv e-prints

Walker, R. C., Ly, C., Junor, W., & Hardee, P. J. 2008, J. Phys. Conf. Series, 131, 012053

Weintroub, J. 2008, Journal of Physics Conference Series, 131, 012047

White, R. L., & Becker, R. H. 1992, ApJS, 79, 331

White, R. L., Becker, R. H., Helfand, D. J., & Gregg, M. D. 1997, ApJ, 475, 479

Wills, B. J. 1975, Australian Journal of Physics Astrophysical Supplement, 38,

Witzel, A., Veron, P., & Veron, M. P. 1971, A&A, 11, 171

Woody, D. P., et al. 2004, in Society of Photo-Optical Instrumentation Engineers (SPIE) Conference Series, Vol. 5498, Society of Photo-Optical Instrumentation Engineers (SPIE) Conference Series, ed. C. M. Bradford, P. A. R. Ade, J. E. Aguirre, J. J. Bock, M. Dragovan, L. Duband, L. Earle, J. Glenn, H. Matsuhara, B. J. Naylor, H. T. Nguyen, M. Yun, & J. Zmuidzinas, 30–41

Wright, A., & Otrupcek, R. 1990, in PKS Catalog (1990), 0-+

Yu, Q., & Tremaine, S. 2003, ApJ, 599, 1129

Zavala, R. T., & Taylor, G. B. 2004, ApJ, 612, 749

Zoonematkermani, S., Helfand, D. J., Becker, R. H., White, R. L., & Perley, R. A. 1990, ApJS, 74, 181